Water Resources Research

Hydraulic Reconstruction of the 1818 Giétro Glacial Lake Outburst Flood

C. Ancey[1] , E. Bardou[2] , M. Funk[3], M. Huss[3] , M. A. Werder[3] , and T. Trewhela[1]

[1]Hydraulics Laboratory, École Polytechnique Fédérale de Lausanne, Lausanne, Switzerland, [2]DSM Consulting, Nax, Switzerland, [3]Laboratory of Hydraulics, Hydrology and Glaciology (VAW), ETH Zurich, Zurich, Switzerland

Abstract In the spring of 1818, ice avalanches from the Giétro Glacier created an ice dam, which in turn formed a glacial lake in the Drance Valley (Canton of Valais, Switzerland). Today, its maximum volume is estimated to have been 25×10^6 m^3. Cantonal authorities commissioned an engineer named Ignaz Venetz to mitigate the risk of the ice dam's failure. He supervised the construction of a tunnel through which a large volume of water was drained as the lake rose (9×10^6 m^3 according to his estimates and 11×10^6 m^3 according to our model). After 2.5 days of slow drainage, the ice dam failed on 16 June 1818 and caused major flooding in the Drance Valley up to 40 km downstream, resulting in about 40 deaths. Venetz's lake monitoring notes, numerous testimonies gathered in the disaster's aftermath, and our field survey have made it possible to collect a wealth of information on this event, which is one of the world's major documented glacial lake outburst floods. Reconstructing major outburst floods remains challenging because not only do they involve enormous volumes of water spreading over long distances but they are also associated with additional physical processes such as massive erosion; intense transport of ice, sediment, and debris; and damage to vegetation and buildings. This paper attempts to reconstruct the 1818 Giétro flood by focusing on its water component. We develop a simple model to estimate the initial hydrograph during the slow drainage and failure phases. The flood's features are deduced by solving the shallow-water equations numerically. The computational framework involves six free parameters, of which five are constrained by physical considerations. Using iterative manual parameter adjustments, we matched the numerical simulations to the historical data. We found that the peak discharge was close to 14,500 m^3/s, the flood's front velocity was about 6 m/s, and flow depth varied considerably along the River Drance's bed (from 30 m just downstream of the ice dam to 2 m on the alluvial fan, 24 km west of the dam). To achieve a good agreement between computations and historical data, we had to select a high value for the Manning friction coefficient n (with n as large as 0.08 s/m$^{1/3}$). As the Drance Valley is narrow, high flow resistance caused the flood's leading edge to behave like a plug, moving at a fairly constant velocity, with little dependence on what happened behind it. This result may explain why a simple flood routing model is able to reproduce the flood's features, because in an Alpine valley, a lateral spreading of the water volume is limited.

Plain Language Summary Every year, natural and man-made dams fail and cause flooding. For public authorities, estimating the risk posed by dams is essential to good risk management. Efficient computational tools are required for analyzing flood risk. Testing these tools is an important step toward ensuring their reliability and performance. Knowledge of major historical floods makes it possible, in principle, to benchmark models, but because historical data are often incomplete and fraught with potential inaccuracies, validation is seldom satisfactory. Here we present one of the few major historical floods for which information on flood initiation and propagation is available and detailed: the Giétro flood. This flood occurred in June 1818 and devastated the Drance Valley in Switzerland. In the spring of that year, ice avalanches blocked the valley floor and formed a glacial lake, whose volume is today estimated at 25×10^6 m^3. The local authorities initiated protection works: A tunnel was drilled through the ice dam, and about half of the stored water volume was drained in 2.5 days. On 16 June 1818, the dam failed suddenly because of significant erosion at its base; this caused a major flood. This paper presents a numerical model for estimating flow rates, velocities, and depths during the dam drainage and flood flow phases. The numerical results agree well with historical data. The flood reconstruction shows that relatively simple models can be used to estimate the effects of a major flood with good accuracy.

Table 1
Significant Glacial Lake Outburst Floods in the Past Two Centuries in Switzerland

Date	Location	V (million m^3)	Q_p (m^3/s)
1818	Giétro Glacier (VS)	20	8,000 to 20,000
1878	Mrjelen Lake, Aletsch Glacier (VS)	10.7	300
1913	Mrjelen Lake, Aletsch Glacier (VS)	4.5	195
1943	Ferpcle Glacier (VS)	1.6	400
1944	Gorner Lake, Gorner Glacier (VS)	6	200
1951	Lower Grindelwald Glacier (BE)	0.135	74.6
1952	Ferpcle Glacier (VS)	0.25	230
1968	Gorner Glacier (VS)	2.9	29
2008	Lower Grindelwald Glacier (BE)	0.57	111
2018	Faverges Lake, Plaine Morte Glacier (BE, VS)	2	80

Note. BE denotes for Canton of Bern and VS for Canton of Valais. Source: Bohorquez and Darby (2008), Haeberli (1983), Huss et al. (2013), Raymond et al. (2003), Walder and Costa (1996), and (Worni et al., 2014).

1. Introduction

Most glacial lakes arise when water is trapped behind moraines during glacier retreat (Clague & O'Connor, 2015; Costa, 1988; Emmer, 2017; Westoby et al., 2014; Worni et al., 2014). They can also form when a glacier bars a valley drained by a water stream or when the glacier front produces ice avalanches that obstruct the valley floor (Clague & O'Connor, 2015; Costa, 1988). Occasionally, they can also be created by melting ice during volcanic eruptions in glacial areas (Costa, 1988).

Ice-dammed lakes are more prone to failure than earthen dams. A survey conducted by Carrivick and Tweed (2016) revealed that 70% of ice-dammed lakes failed but only 9% of moraine-dammed lakes. Ice dams are composed of bulk materials (ice or mixtures of ice and rocks), which are permeable and of varying density. Consequently, an ice dam's stability is often poor, and its failure may be rapid (within tens of minutes), generating large floods commonly called *glacial lake outburst floods* (and sometimes *jökulhlaups*). Not all glacial lakes produce large floods—sometimes partial drainage occurs, often in a quasiperiodic way (Costa, 1988; Dussaillant et al., 2010; Walder & Costa, 1996). When failure does occur, either or both of the following mechanisms are at work: (i) As a result of the melting ice, drains pierce the ice dam, and their growth leads to exponentially rising runoff (Flowers et al., 2004; Nye, 1976); and (ii) water pressure or overflow leads to the formation of a breach and dam failure (Walder & Costa, 1996).

With global climate change, the risk of glacial lake outburst floods has been increasing in recent years (Carrivick & Tweed, 2016; Harrison et al., 2018). Switzerland is a mountainous country with a significant ice cover (944 km^2, or 2.3% of its surface area, covered by glaciers in 2010). Switzerland has been concerned by glacial lake outburst floods over the last few centuries (Fischer et al., 2014; Raymond et al., 2003; Werder et al., 2010), as shown in Table 1. The 1818 Giétro flood—the focus of this paper—was the most significant of these floods, and as will be discussed in section 5.1, it was one of the world's largest documented glacial lake outburst floods. With respect to other glacial hazards that have the potential to affect valley floors, glacial lake outburst floods can affect larger areas as they involve the movement of huge volumes of water over long distances from the source point. The risk to people and property is thus high, especially in heavily populated areas (Carrivick & Tweed, 2016).

Today, higher densities of population and sensitive infrastructure (such as hydropower plants and international roads) spur national and local authorities to take a closer look at the threats posed by the potential failure of natural and man-made dams. When perceived as unreliable by the population, risk analyses fuel controversies rather than resolving them. A typical example in Europe is the Vouglans reservoir dam at the French-Swiss border; its failure could cause a Fukushima-like accident if the Bugey nuclear plant downstream were flooded. In this context, making well-informed decisions calls for specific computational tools that can describe the release and flow of large volumes of water. These tools require testing against documented historical events to demonstrate their reliability. In this paper, we will focus on the major flood of
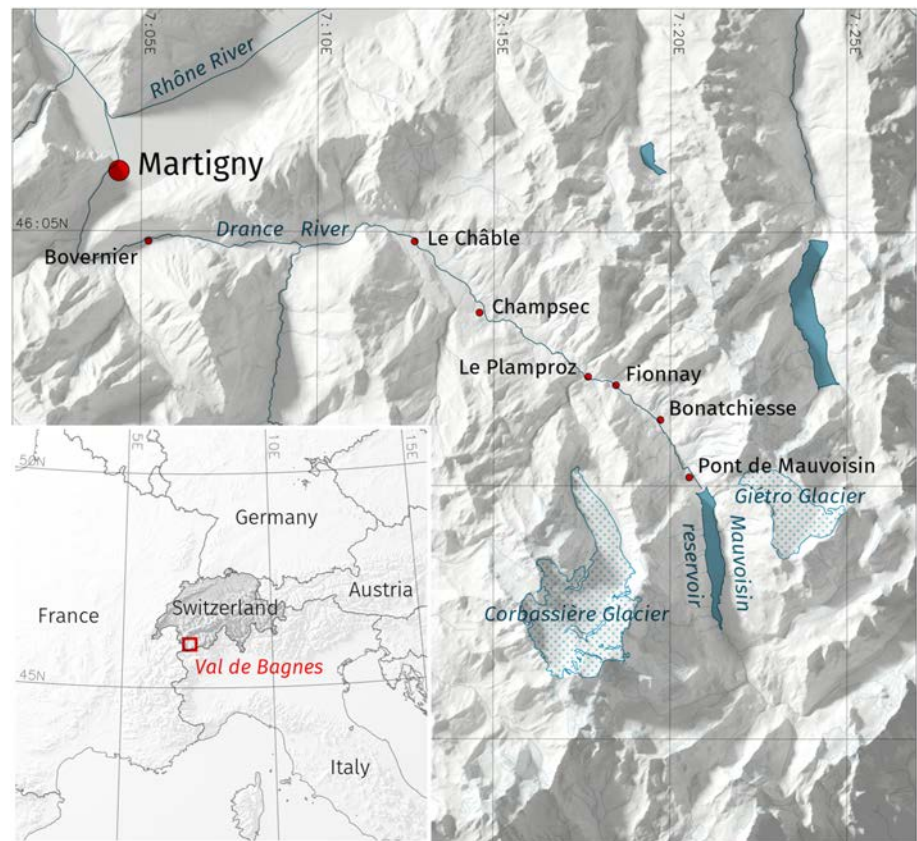
Figure 1. Location map of the Drance Valley and the Giétro glacier, Canton du Valais (Switzerland). The upper part of this valley is called the *Val de Bagnes*. The River Drance's longitudinal profile is shown in Text S1. We also show the different hamlets and villages that the River Drance flows through and for which we have historical information about the 1818 flood. That year, the glacial lake created by ice avalanches from the Giétro Glacier occupied nearly the same location as the Mauvoisin reservoir does today (bottom right).

the River Drance (also spelled *River Dranse*) in the Canton of Valais (Switzerland; see Figure 1), caused by the sudden drainage of a glacial lake formed by ice avalanches from the Giétro (sometimes spelled *Gitroz*) Glacier in June 1818. The Giétro's historic major flood can provide a test case with which to supplement the few other documented cases such as the Ha! Ha! dike-break flood (Capart et al., 2007; El Kadi Abderrezzak et al., 2011; Lapointe et al., 1998), the Sella Zerbino dam break (Petaccia et al., 2016), and the Malpasset dam break (George, 2011; Hervouet & Petitjean, 1999; Mulder et al., 2009; Valiani et al., 2002).

A considerable body of literature has been devoted to flood routing and dam breaking (Carrivick, 2010; Chanson, 2004; Cunge et al., 1980; ICOLD, 1998; Vreugdenhil, 1994; Wu, 2007). Glacial lakes add complexity to the physics of dam-break floods. Steep glacial terrain implies that floods are associated with intense ice, rock, and bedload transport, causing massive bed aggradation and degradation. Sediment transport may take the form of landslides or debris flows, whose rheological behavior differs significantly from that of water alone. How the dam breaks and how water is released are also of paramount importance to accurately predicting a flood's features. Yet there is often no definite information on the dam's inner structure, the cause of failure, how long it took for the dam to break, and the volume of water that was drained from the lake or reservoir. Furthermore, the assumptions about energy dissipation and pressure distribution that are routinely used in computational hydraulic models are more questionable when used for irregular topography and steep terrain (Castro-Orgaz & Hager, 2017), especially when flows transport large volumes of debris. All in all, modeling glacial lake outburst floods remains a challenging task.

Faced with the complexity of the processes involved and their related uncertainties (in terms of process knowledge and the relative paucity and inaccuracy of field data), it is tempting to start modeling the Giétro outburst flood using the simplest computational framework possible and then analyzing the strengths and

weaknesses of this first-order approach. Here we will focus solely on the hydraulic component (the water flow), thereby ignoring the parts played by additional processes such as sediment transport and terrain erosion. Furthermore, in order to center the paper on describing the 1818 Giétro flood and its hydraulic reconstruction, we have left out the computational detail. Additional information and proofs are presented in supporting information, and readers can follow the cross-references to find further supporting material. All the data, along with a Mathematica notebook for computing the initial hydrograph, can be obtained from the data repository (see Acknowledgments).

2. Data, Site, and Chronology of the Disaster

2.1. Historic and Geomorphological Data

The 2018 commemorations of the 1818 disaster gave rise to research actions involving scientists from various disciplines (history, geomorphology, glaciology, hydraulics, and risk analysis; Payot & Meilland, 2018a, 2018b). The material collected on this occasion provided a wealth of information, which has been used for reconstructing the 1818 outburst flood. There are four main sources of knowledge available today:

- Testimonies in archives. As of April 1818, the lake was surveyed by the Cantonal Engineer, Ignaz Venetz (see section 2.3). Venetz was a remarkable engineer and naturalist, whose physical intuition and acute sense of observation were decisive in many engineering problems. His field observations gave rise to the first theory of glaciers (glacial theory was subsequently developed by Louis Agassiz; Balmer, 1970; Mariétan, 1959). From his field visits, Hans Conrad Escher von der Linth provided a detailed account of what happened before and after the dam failure, and he collected numerous testimonies. Escher von der Linth was a Swiss scientist with a good background in hydraulics (among other responsibilities, he was in charge of mitigating floods on the River Linth by channeling the streambed); his figures should be deemed trustworthy (ASSHS, 2014). Pastor Philippe-Sirice Bridel also made field trips to Giétro before and after the disaster. Other testimonies in the cantonal archives have provided further information on the extent of the flood (Corboz, 2015; Payot & Meilland, 2018a, 2018b). See section 2.4 for full details of the information used from the archives.
- Damage to buildings. A group of historians has collected all the relevant data related to buildings and man-made structures damaged during the flood (Payot & Meilland, 2018a).
- Geomorphological clues. The outburst flood involved massive volumes of sediment and debris of all sorts, undermined talus slopes, and eroded the valley bottom. Some of the coarsest boulders were deposited in the upper Val de Bagnes. However, it is difficult to identify and date every change that occurs in natural terrain. For instance, rockfalls and avalanches (entraining rocky debris) are also frequent in the narrow upper valley, and their deposits may be confused with those left by the 1818 flood.
- Meteorological data. These data were needed when estimating the runoff over the watershed in the months preceding the disaster using the Glacier Evolution Runoff Model (GERM). We used air temperature and precipitation data from the Grand-Saint-Bernard weather station. Located 20 km west of the Giétro ice-dam at an elevation of 2,470 m, this station has been in operation since October 1817 and thus provides an approximation of the weather conditions in the neighboring Drance Valley.

2.2. Location

The Giétro Glacier is located in the upper part of the Val de Bagnes (see Figure 1). In 2010, the glacier was 4.5 km long and covered an area of 5.2 km^2, descending from 3,820 to 2,640 m above sea level (asl), under the northern face of the Ruinette (3,875 m asl; Fischer et al., 2014). It is a medium-sized mountain glacier, whose accumulation zone extends over a relatively flat area (with a mean slope of 28%). By contrast, its front moves over steep bedrock (its mean slope is 58% in the 1,950 to 2,850-m elevation range). Whereas the glacier's front currently sits at a high elevation (2,760 m asl) and is receding every year, it has long been moving forward and backward, depending on the ice mass balance in its upper cirque. When the glacier's front hung over the steepest part of the bedrock, it produced ice avalanches which came to a halt in the valley floor, currently occupied by the Mauvoisin reservoir ("Mauvoisin" is a contraction of "mauvais voisin" in French, that is, "bad neighbor," a toponym reflecting that the Giétro Glacier's vicinity was unloved by the valley's inhabitants at that time). Figure 2 shows the current Mauvoisin reservoir (with its arch dam just downstream of the Giétro gully), whose mean volume is 211×10^6 m^3. In 1818, the ice dam's apex was aligned with the gully.

Figure 2. View of the Giétro site. Today, the valley floor is occupied by the Mauvoisin reservoir. The receding glacier front is hardly visible at the top of the gully incising the western face of the Ruinette. The Mauvoisin dam is the highest arch dam in Europe (with a height of 250 m relative to the valley bottom). By comparison, the ice dam was 80 m tall.

2.3. Chronology of a Disaster

During the Little Ice Age, the Giétro Glacier produced ice avalanches more frequently than during warm periods (Holzhauser & Zumbühl, 1999). Their deposits fed a regenerated glacier, which at times could bar the River Drance. Before the 1818 disaster, glacial lake outburst floods had devastated the Drance Valley down to its confluence with the River Rhone at least three times (Raymond et al., 2003): on 7 August 1549, on 25 May 1590 in a scenario close to that of the 1818 event (140 persons killed and about 500 buildings destroyed), and in 1680 (with no further information on the damage and death toll).

Between 1805 and 1818, summers were cold and wet, and the Giétro Glacier progressed toward the valley floor once more. In 1816, sometimes called the "year without a summer," temperatures were anomalously cold—"2 to 4 °C below the 1951–1980 reference period" (Luterbacher & Pfister, 2015). Intense ice avalanche activity formed an ice cone which obstructed the river (see Figures S3 and S4). Initially, the water stream found its path underneath the ice dam, but creeping ice caused the passage to shrink progressively, eventually giving rise to a glacial lake upstream of the dam. On 27 May 1817, this lake experienced rapid drainage, but the resulting flood did not cause any damage.

In the spring of 1818, the ice dam grew considerably, and the lake formed again. The ice dam dimensions impressed witnesses: 600 ± 100 m wide at its base and 90 m high on the left (westward) side relative to the valley floor. Its right (eastward) side extended up to the Giétro Glacier. The total ice volume was estimated to be 10 million cubic meters. By early May 1818, the lake volume had already reached unusually large dimensions, estimated to be 5×10^6 m^3, and it was continuing to fill quickly with water resulting from snowmelt. From 10 May to 13 June 1818, the lake's depth increased by 22 m.

In late April 1818, the River Drance's discharge was vanishingly small at Fionnay, a village 5.5 km downstream of the ice dam. Informed by the local peasants in early May, the Canton du Valais' authorities dispatched a delegation headed by the Cantonal Engineer, Ignaz Venetz, on 9 May. His mission was to evaluate the risk posed by the lake and propose countermeasures (Gard, 1988; Payot & Meilland, 2018a). Venetz feared that the lake surface would reach the top of the ice dam and spill over it. The mitigation solution outlined by the local authorities was to trench the dam to create a spillway. Venetz' strategy was simpler: digging a 195-m long, 1.9-m high, 1.3-m wide tunnel into the ice dam, through which the lake waters would flow, 23 m below the top of the dam. A series of fire signals was set up from Giétro to Monthey, far down the River Rhine, to warn people of an eventual dam failure, and furthermore, bridges were removed along the River Drance. Tunneling work started on 11 May and was completed on 4 June 1818 despite adverse weather conditions and intense snow avalanche activity. The lake level reached the tunnel entrance on 13 June at 10 p.m., but ice blocks soon started clogging the tunnel entrance. These were removed by a courageous worker.

Initially, everything happened as expected: The water drained through the tunnel at a sufficiently high flow rate to lower the lake level by 30 cm within 7 hr (see Table 2). Under the effect of ice melting and mechanical erosion, the free-surface water flow progressively eroded the tunnel walls and floor, causing it to widen

Table 2
Water Level Variation Relative to the Maximum Water Level

Time	Water level variation
13 June 1818, 10:00 p.m.	Water penetrated the tunnel
13 June 1818, 11:00 p.m.	Water level increased a little
14 June 1818, 5:00 p.m.	30-cm decrease
15 June 1818, 6:00 a.m.	3.2-m decrease
16 June 1818, 6:00 a.m.	9.7-m decrease
16 June 1818, 4:00 p.m.	14.6-m decrease
16 June 1818, 4:30 p.m.	The dam failed

Note. Source: Gard (1988) and Escher von der Linth (1818).

and drop with the water level. A cascade poured from the tunnel exit. By 16 June at 4 p.m., the lake level had decreased by 14 m, and thereby a volume of 9×10^6 m^3 had been drained according to Escher von der Linth (1818), who provided a detailed record of the water level (see Table 2). At that moment, something unexpected occurred: Upon reaching the talus made of fallen rocks, the cascade began to scour the foot of the slope bearing the ice dam, and the incision through the dam, created at the downstream end of the tunnel, gradually sliced inward (see Figure 3). On 15 June, at 6 a.m., the incision in the dam wall created by the cascade was 25 m deep, and part of the talus had been entrained (Mariétan, 1959).

On 16 June, at 4:30 p.m., the ice wall at the tunnel entrance broke. The exact scenario is unknown, but on the basis of an eyewitness account, Escher von der Linth (1818) wrote "the part of the glacier that formed the lake wall saw its thickness shrink to the point that the length of the tunnel bottom, which was initially 608 feet [195 m], had decreased to 8 feet [2.5 m] when the lake breached the glacier. It is, however, not the failure of this thin ice wall that caused the outburst flood. It arose from another process. When the cascade had incised a gully a few hundred feet deep into the lower part of the glacier, it (…) scoured the layers of fallen rocks." We can imagine that talus scouring and dam undercutting destabilized the ice mass (there was a cantilever failure). Under the pressure of the remaining water volume, dam failure occurred rapidly. According to the testimonies, it took from 30 to 35 min for the lake to drain (Gard, 1988).

Finding refuge on higher ground near Fionnay, Venetz and his companions saw a huge mass of mud, boulders, and trees, preceded by a cloud of dust and vapor, rushing down the valley with a roaring noise. It took 1 hr 30 min for the flood front to reach Martigny, 33 km away from Giétro, and 6 hr 30 min to reach Lake Geneva. The front velocity was about 24 km/hr on average. Table 3 gives the times at which the flood struck the main villages. The flood killed 40 people (there are different views on this figure because of the presence of foreign workers and travelers, whose disappearance did not necessarily mean that they had been killed). All in all, it also destroyed 38 dwellings, 336 other constructions, and 17 bridges. In the years after the 1818 disaster, the Giétro Glacier continued to loom over the Val de Bagnes. Venetz found a clever way of keeping a trench open through the ice dam so that a trickle of running water was sufficient to melt the ice and keep the trench clear (Venetz, 1821, 1825).

A comparison between the 1595 and 1818 floods shows that the cantonal authorities had learned much from the first disaster. In 1595, the death toll was 140 (which is the largest ever death toll due to an outburst flood
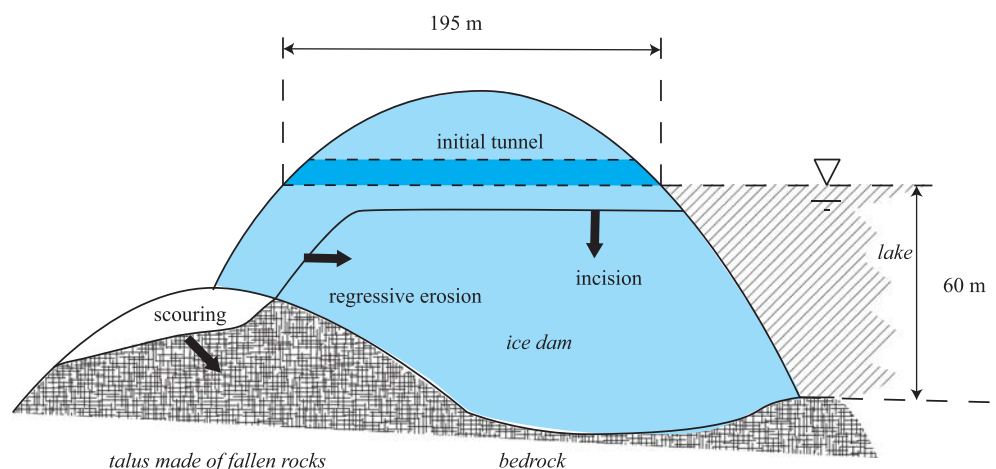

Figure 3. Sketch of the ice dam pierced by the tunnel. Three processes were at work. The heat convected by the water flow melted the tunnel walls and floor, causing it to lower. Because of the water's high speed, a cascade formed at the downstream end of the tunnel. This cascade caused regressive erosion and scouring. We also mention the tunnel dimensions given by Escher von der Linth (1818). The dashed lines show the initial tunnel position, whereas the solid line shows the tunnel-bottom position at a given time t during the slow drainage phase. The sketch is inspired by a drawing by pastor Gilliron (Gard, 1988). The drawing is not to scale (the talus, in particular, has been enlarged).

Table 3
Front Position Over Time

Location	Time	Maximum flow depth (m)
Giétro (dam break), 1,800 m	4:30 p.m.	30
Champsec, 906 m	5:00 p.m.	13
Le Châble, 821 m	5:05 to 5:10 p.m.	13–15
Martigny	6:00 p.m.	2–3
Saint-Maurice	7:00 p.m.	
Noville (Lake Geneva)	11:00 p.m.	

Note. The maximum flow depth is also given. Because the town of Martigny sprawled over a large area (the River Drance's alluvial fan), the precise point reached by the flood front at 6:00 p.m. remains unclear. Source: Corboz (2015), Escher von der Linth (1818), Gard (1988), and Payot and Meilland (2018a).

in Switzerland). With seven inhabitants per square kilometer (population per square kilometer) in 1595 and 12 population per square kilometer in 1818 (compared with 65 population per square kilometer today), the Canton of Valais was still sparsely inhabited, but it had seen its population double over the previous two centuries (Mathieu, 2000). In this respect, one could reasonably consider that Venetz's measures saved more than 200 lives. Switzerland was still a young federal country in 1818 (Valais only joined the Confederation in 1815), but an upsurge of national solidarity made it possible to help 1,268 families and to reconstruct the Val de Bagnes quickly after the disaster (Payot & Meilland, 2018a).

Nevertheless, the mitigation strategy had not been without shortcomings. Even though he implemented an efficient strategy, Ignaz Venetz did not have all the tools at his disposal for optimizing lake drainage. At the time, it was impossible for him to anticipate that ice melt would cause such substantial regressive erosion and scouring and thus lead to dam failure. The death toll was also made higher because the fire signals were not activated on time (false alarms in the preceding days had made inhabitants less wary, and the complete dam failure took only a few minutes to occur).

2.4. Key Values

The archives give estimates of water volumes, ice heights, and the times taken for lake drainage and flooding. Among others, Escher von der Linth received first-hand information from Venetz, allowing him to give many quantitative details. He wrote "According to the unanimous testimonies from inhabitants, this flood lasted approximately half an hour, wherever it passed; so, within thirty minutes, the entire water mass, mobilizing all debris and involving a volume exceeding 530 million cubic feet, passed through every section of the valley. Every second, the outburst flood provided 300,000 cubic feet of water." In Switzerland at that time, a foot could measure between 26 and 36 cm depending on the canton (the metric system was enforced nationally in 1868), but the French foot (0.324 cm) was the most common in western Switzerland (ASSHS, 2014). The above quotation from Escher von der Linth means that the volume drained during the failure phase was about 18×10^6 m^3, and the mean water discharge reached 9,600 m^3/s. The maximum lake volume was estimated at 27.2×10^6 m^3 and its mean depth at 60 m. Table 3 summarizes the data related to lake level, flood front movement, and maximum flow depths. All these data are fraught with uncertainty, and it is difficult to make an appreciation of their accuracy. For instance, Escher von der Linth stated that the tunnel length was 608 feet long (195 m), whereas Pastor Gilliron indicated a length of 685 feet (219 m). As Escher von der Linth was a trained scientist with considerable experience in hydraulics and was in touch with Venetz, we decided to go by his descriptions. The time indications may also be questionable: The sole clock along the length of the River Drance was the one installed in Bagnes' church clocktower in 1810. Watches were luxury goods that would have been of little use to the Val de Bagnes' inhabitants at that time (Dubuis, 1993). Yet the disaster foretold had attracted officials, engineers, and some curious tourists who would have been wealthy individuals from large industrial cities. It would have been likely that a few of them had the presence of mind to look at their pocket watches. Again, it is difficult to estimate the uncertainties on flood timing.

3. Computational Methods

To reconstruct the Giétro outburst flood, we have considered two different steps:

- In the first step (drainage), we consider how the lake had drained until the ice dam breached, and we compute the initial flood hydrograph resulting from the dam failure. This provides the upstream boundary condition for the flood routing model.
- In the second step (flood propagation), we compute how the water volume released from the Giétro lake flowed along the Drance valley by solving the shallow-water equations numerically.

3.1. Drainage and Dam Break

For embankment and moraine-dammed lakes, there are two main approaches to computing dam failure: (i) numerical models based on mass and momentum balance equations supplemented by erosion laws (Begam et al., 2018; Castro-Orgaz & Hager, 2013; Faeh, 2007; Larocque et al., 2013), and (ii) conceptual models based on a series of differential equations accounting for the various processes at play (Capart, 2013; Peter et al., 2018; Walder & O'Connor, 1997). For ice-dammed lakes, the water's change phase should also be considered. To the best of our knowledge, only conceptual models of ice dam failure have been developed (Clarke, 1982; Carrivick et al., 2017; Kingslake et al., 2015; Nye, 1976; Ng & Björnsson, 2003; Vincent et al., 2010; Walder & Costa, 1996).

Lake drainage by down-cutting, open-channel flow has been extensively studied and modeled (Walder & Costa, 1996; Vincent et al., 2010; Kingslake et al., 2015). To the best of our knowledge, the mechanical erosion and sudden failure of an ice dam have so far not been documented. The Giétro ice dam added two further elements of complexity:

- The dam was a regenerated glacier, which did not have the structural integrity that "normal" ice dams have. The accumulated ice debris had probably not completely fused to solid ice.
- The waterfall at the tunnel exit caused backward incision and weakened the talus foundation, whose failure was likely the triggering event that caused the dam failure. Backward incision has been studied in the context of ice channels exhibiting a step-and-pool morphology (Vatne & Irvine-Fynn, 2016), that is, on small spatial scales (typically, with waterfall heights of 1 m). For the Giétro dam, the waterfall height was tens of meters high.

Given the complexity of the processes at play, we have thus developed a conceptual model of drainage to compute the hydrograph before and when the dam breached. We consider two stages of drainage:

- During the *slow drainage stage*, the lake overflow was evacuated via the tunnel. Owing to ice melt, the tunnel's dimensions were increasing. According to testimonies, this phase lasted 66.5 hr (from 10:00 p.m. on 13 June to 04:30 p.m. on 16 June).
- The *fast drainage stage* was caused by the dam failure, which occurred at 04:30 p.m. on 16 June. The lake was drained within 30 to 35 min, according to testimonies (Gard, 1988).

The equations used in the hydrograph computation are derived in the Appendices A and B. Here we merely summarized the main assumptions and equations.

In this model, the lake behaves like a reservoir whose water level varies as a result of water supply (melting snow) and lake drainage. We wish to compute the water level z_l, the flow depth h in the tunnel, and this tunnel's width w_s and entrance elevation z_s. The water level z_l satisfied an ordinary differential equation expressing mass balance:

$$\frac{dz_l}{dt} = \frac{Q_{in} - Q_{out}}{A}, \tag{1}$$

where Q_{in} is the inflow rate and Q_{out} is the outflow rate. The lake's free-surface area is denoted by $A(z_l)$. This function was computed by digitizing the contour lines of the Siegried map, which was Switzerland's official, published as of 1870, at a scale of 1:50,000 for the Alps and with contour lines every 30 m. Although the Drance Valley was mapped in 1878, glacial retreat had just started, and thus, despite the 60 years separating the Giétro disaster and mapping, the Siegfried map provides a fair interpretation of glacial cover in 1818.

The watershed covers an area of 105 km^2 and had an ice cover approaching 50% in 1818. Water runoff arising from snowmelt and precipitation was estimated using the glacio-hydrological GERM (Huss et al., 2008). For

the computations, we fitted a power law function to the GERM data $V(t)$, where V denotes the lake volume at time t. The incoming flow rate was estimated as $Q_{in}(t) = \dot{V}(t)$.

During both phases, we assume that the sudden flow contraction at the tunnel/trench entrance caused that flow to become locally critical. As a first approximation, we assume that the outflow rate was given by

$$Q_{out} = c_d w_s \sqrt{g \delta z^3}, \tag{2}$$

where w_s is the tunnel width, g the gravitational acceleration, $\delta z = z_l - z_s$ the water flow depth at the tunnel entrance, and z_s the tunnel elevation (Chow, 1959; Hager, 2010). For ideal flows, the discharge coefficient is $c_d = c_{d0} = (2/3)^{3/2}$, but here, head losses and contraction effects led us to select a lower value $c_d = 0.7c_{d0} \sim 0.38$ (Hager, 2010; Hager & Dupraz, 1985; Hager & Schwalt, 1994). The initial condition is $z_{s,0} = 1,860$ m asl so that the initial volume stored in the lake is 25.6×10^6 m³ (just before the slow-drainage phase started) and the initial lake depth is 60 m, consistent with the values cited by Escher von der Linth (see section 2.4).

During the slow-drainage phase, the water flow along the tunnel is described as a free-surface flow in a prismatic channel of slope i, width w_s. We assume that quickly after entering the tunnel, the flow reached its normal depth h (we neglect spatial variations in h in the tunnel). Wall friction is assumed to follow a Darcy-Weisbach equation, with a wall friction coefficient f given by Yen's (2002) equation. Ice roughness is denoted by k_s. Lake temperature T_l was slightly above melting point. During its flow in through the tunnel, the water nevertheless convected heat. A small part of that heat was extracted and melted the ice walls. By assuming that the entire heat flux q was used to that end (and thus there was no heat conduction through the ice layers), we deduce the incision rate to be

$$\dot{z}_s = -\frac{\chi q}{\varrho_i (w_s + h\Gamma)L}, \tag{3}$$

where z_s is the tunnel entrance elevation, $\chi = h + 2w_s$ is the wetted perimeter, L the latent heat, ϱ_i ice density, and $\Gamma = -\dot{w}_s / \dot{z}_s$ an empirical coefficient relating lateral and vertical incision rates. We use the Gnielinski empirical equation to relate the heat flux to the water flow parameters (Bergman et al., 2011).

During the fast-drainage phase, the thermodynamically controlled incision process is replaced by mechanical erosion. The precise details are unknown, of course, but we assume that the breach dimensions continued to increase until the incision reached the bedrock located at $z_{bed} = 1,800$ m asl. We assume that the vertical incision rate is

$$\dot{z}_s = -e\bar{u}^2, \tag{4}$$

with $\bar{u} = Q_{out}/(w_s h_c)$ the mean velocity, e an empirical mechanical erosion factor, and $h_c = 2(z_l - z_s)/3$ the critical flow depth. We still assume that the lateral incision rate is given by $\dot{w}_s = -\Gamma\dot{z}_s = e\Gamma\bar{u}^2$. Once the bedrock has been reached in the simulations, the erosion rate is shut off: $e = 0$.

In the end, the model has five free parameters: lake temperature T_l, tunnel slope i, ice roughness k_s, incision rate parameter Γ, and mechanical erosion factor e. The values of the first four parameters are constrained by physics (T_l is close to 0 °C, i is close to 0, $k_s = O(1)$ mm, and $\Gamma = O(1)$). The fifth parameter (e) is empirical and reflects the numerous processes that occurred during the failure phase. We selected them so that model predictions matched historical data.

3.2. Flood Routing

We used the shallow-water equations to model the outburst flood from the glacial lake to the River Rhone, 40 km west of the Giétro Glacier. The equations were solved numerically using the finite-volume Iber code (Bladé et al., 2014; Cea & Bladé, 2015). This is a two-dimensional hydrodynamic model based on unstructured meshes and on a first- or second-order Roe solver for the flux terms in the shallow-water equations. Iber also includes additional modules (such as depth-averaged turbulence, sediment transport, and runoff) that we did not use for the Giétro flood. Bed friction is modeled using the Manning equation, with the Manning coefficient $n = 0.08$ s/m$^{1/3}$ applied to the whole domain.

We used various sources of data to model the topography. We began by using a low-resolution digital elevation map (DHM25 grid, equivalent to a 1:25,000 scale map, with a 25-m spatial resolution). We then refined the elevation model over a 400-m wide band centered on the streambed path using LIDAR data (SwissAlti3D
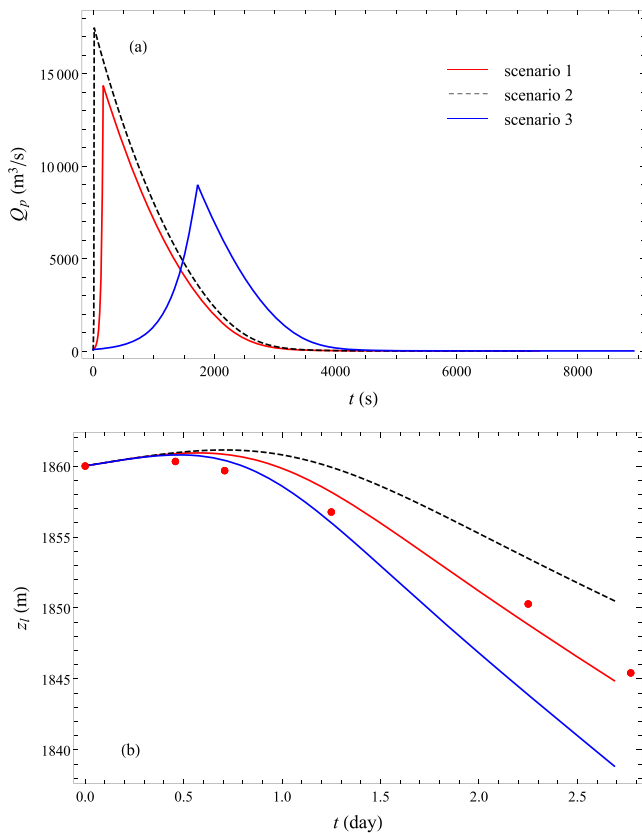
Figure 4. (a) Hydrograph of the fast-drainage phase when the ice dam is failing. The hydrographs are obtained by solving equations (1)–(3) (rising limb) or (1), (2), and (4) (falling limb). For Scenario 1, we used the following parameters: $T_l = 1°C$, $i = 1\%$, $k_s = 1$ mm, $\Gamma = 2/3$, and $e = 0.005$ s/m. For Scenario 2, we used the following: $T_l = 0.75°C$ and $e = 0.05$ s/m, and the other parameters were the same as for Scenario 1. For Scenario 3, we used the following: $T_l = 1.25°C$ and $e = 5 \times 10^{-4}$ s/m. Time from dam failure (4:30 p.m. on 16 June 1818). (b) Time variation in the lake's water elevation z_l for the three scenarios considered. The dots show the data provided by Escher von der Linth (1818) and summarized in Table 3. Time from start of drainage (10:00 p.m. on 13 June 1818).

grid, with a 2-m spatial resolution). All the files were provided by the Swiss Federal Office of Topography (SwissTopo) and corresponded to the most up-to-date topography of the Drance Valley. In the absence of bathymetric information, the Mauvoisin reservoir was not covered by the digital elevation model, but as we used a hydrograph as the boundary condition, this was not needed. From 1818 to 2018, the landscape has considerably evolved, especially in the upper part of the Val de Bagnes (at the village of Fionnay, due to the building of a hydropower plant and a buffer lake) and at its lowest part (urbanized areas of the town of Martigny). Gravel extraction upstream of the village of Sembrancher has also altered bed topography. Over much of its length, however, the streambed has not been significantly modified or engineered. We have partial historical information relating to the Val de Bagnes' topography in the nineteenth century. Although the cadastral surveys of the Canton du Valais and the Dufour map (undertaken in the 1850s) do not provide topographic information, they locate numerous place names which were useful to give spatial context to testimonies. We used the Napoleon map (dating from the early nineteenth century) to smooth the River Drance's alluvial fan topography near Martigny (which is entirely urbanized today), whereas we incised the Drance's channelized bed.

The digital elevation model was tailored to fit the Drance Valley and then meshed using irregular triangles. Its surface was about 307 km². For most of the runs presented here, the mesh involved 985,000 triangles (in other words, the mean triangle-side length was 25 m, but smaller triangles were used when topography varied significantly over short distances along the river). Using an Intel Core i7-6700 processor (3.4 GHz, 4 cores), simulating the flood motion from the Giétro lake to the River Rhone took 4 hr. Additional tests were conducted with a mesh based on 6 million triangles with no noticeable change in the numerical results (but with far longer run times).

4. Results

4.1. Dam Failure
We studied three scenarios.

- Scenario 1 is consistent with the testimonies collected by Escher von der Linth regarding the time variation in the lake's water level (see Table 2) and the dam failure's duration. We selected the following values: lake temperature $T_l = 1°C$, tunnel slope $i = 1\%$, ice roughness $k_s = 1$ mm, incision rate parameter $\Gamma = 2/3$, and mechanical erosion factor $e = 0.005$ s/m. The latter coefficient was adjusted by trial and error until the hydrograph's duration was close to 30 min.
- Scenario 2 differs from Scenario 1 by $T_l = 0.75°C$ and $e = 0.05$ s/m. This scenario is close to instantaneous dam failure. Indeed, by lowering water temperature, we made tunnel incision less marked than for Scenario 1, thus causing a slower decrease in the water level during the slow drainage phase (about −10 m for Scenario 2 against −15 m for Scenario 1). During the fast drainage phase, the higher value (10 times faster than Scenario 1) led to a higher peak discharge (about 17,500 m³/s for Scenario 2 vs. 14,400 m³/s for Scenario 1) and shorter hydrograph duration.
- Scenario 3 differs from Scenario 1 by $T_l = 1.25°C$ and $e = 5 \times 10^{-4}$ s/m. We sought the opposite effects relative to Scenario 2: Increasing water temperature leads to higher discharges during the slow-drainage phase, while decreasing the mechanical erosion rate e stretches the hydrograph: Its peak discharge is much lower (about 8,900 m³/s for Scenario 2 vs. 14,400 m³/s for Scenario 1), and duration is longer (about twice as long).

The last two scenarios are not consistent with the description given by Escher von der Linth, but they make it possible to test how sensitive the numerical results are to changes in the model parameters (see the
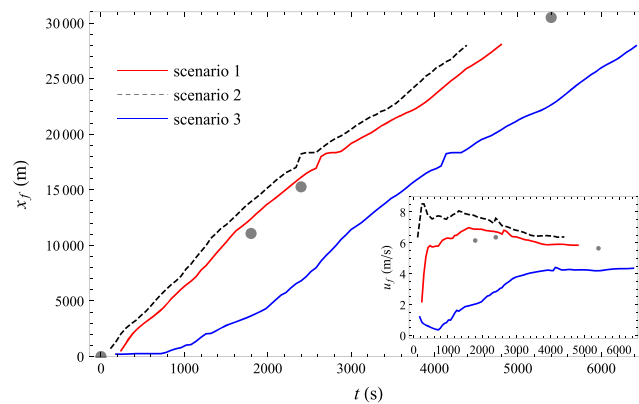
Figure 5. Front position x_f over time t for each scenario. The gray points show the front positions according to testimonies (see Table 3). The inset shows the mean front velocity (after dam failure) $u_f = x_f/t$. Computations done for $n = 0.08$ s/m$^{1/3}$. We show only the computed front position before the flood reached the alluvial fan in Martigny.

supporting information). Figure 4a shows the resulting hydrographs. Figure 4b shows that Scenario 1 reproduces the lake's water elevation in the slow-drainage stage, whereas Scenarios 2 and 3 lead to significant deviations. As the temperature is lower and the mechanical erosion factor e is larger in Scenario 2 than in Scenario 1, the peak discharge is higher, and the volume drained during the fast-drainage stage is larger. Conversely, Scenario 2 produces lower peak discharge and flood volume.

4.2. Flood Front

Among the available historical information, the flood's front position is likely the one that is least subject to uncertainty. Figure 5 shows the front position x_f as a function of time. The inset shows the mean front velocity (computed from dam failure) $u_f = x_f/t$ and compares it with the historical information (deduced from Table 3). Until it arrived at the alluvial fan's apex in Martigny, the flood followed the River Drance, which incised the narrow valley's floor. It is thus easy to define the front as the furthest point reached along the streambed. On the alluvial fan, the flood spread out until the water occupied all the available space. During the spreading phase, it is difficult to determine a unique front point. Consequently, we show only the front positions before the flood reached the alluvial fan (that is for $x_f \leq 3 \times 10^4$ m).

Except for Scenario 2, there is a lag time in front motion early on in the flood. This latency phase is especially marked in Scenario 3: During the first 12 min, the front has not moved very far. Its velocity is quite low (less than 1.5 m/s). A similar trend is observed in Scenario 1. After this low-velocity phase, the front accelerated vigorously and reached a fairly constant velocity. In Scenario 1, this front velocity is about 6 m/s, in close agreement with the observed mean velocity deduced from testimonies (ranging from 5.8 to 6.2 m/s).

Interestingly, although the mean velocity $u_f = x_f/t$ varies from one scenario to another, the instantaneous velocity defined as $\dot{x}_f = dx_f/dt$ is reasonably constant for times beyond 2,000 s, regardless of the scenario (see Figure S24). This constancy is reflected by the slopes of the the $x_f(t)$ curves which are fairly similar. The difference in the mean velocity arises mainly from the initial lag time. The hydrograph shape thus has a significant influence on front motion early on in the failure, but this influence wanes with time.

In the data repository, we provide two videos showing the front progression for Scenario 1 (with an indication of the flow depth and velocity for the body of water behind the front).

4.3. Hydrograph

Figure 6 shows the flood hydrographs computed for the three scenarios at different locations along the River Drance. There is not much difference between Scenarios 1 and 2. The rising limb remains steep over time because of the high roughness coefficient $n = 0.08$ s/m$^{1/3}$ chosen for the simulations and, as shown below (see section 5.4), n controls the front dynamics to a large extent. To begin with, the peak discharge decreases significantly from 15,000 to 5,000 m^3/s for $t > 1$ hr. This reduction causes the falling limb to stretch, and so the hydrograph's duration increases as the front moves further forward. Escher von der Linth stated that the flood's duration remained constant (30 min) all along the River Drance. This temporal constancy is not seen in the numerical simulations, however. For Scenario 3, the rising limb steepens quickly after the Mauvoisin
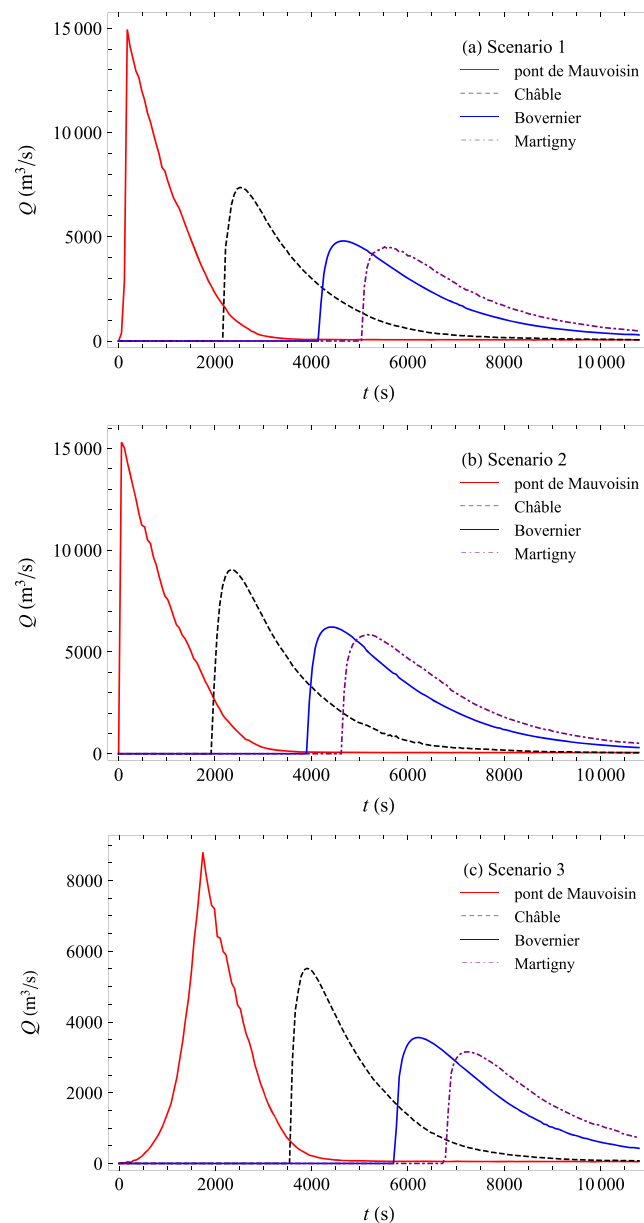
Figure 6. Flood hydrographs at the pont de Mauvoisin (Mauvoisin bridge), Champsec, Le Châble, and Martigny. For each scenario ((a) Scenario 1, (b) Scenario 2, and (c) Scenario 3), the initial hydrograph at the ice dam is the one shown in Figure 4a.

bridge, which reflects the large volume of water accumulated behind the front, which generated waves that caught up with the front.

4.4. Flow Depth

Figure 7 shows the longitudinal profile of the maximum flow depth for each scenario. Historical information is also shown (see Tables 3 and S1). For Scenario 1, the computed maximum flow depths match the field and historical data except for Point 5 (the Fionnay gorges). Fionnay's surroundings have changed significantly since the nineteenth century: In 1818, the Giétro flood caused the slope failure of the scarps above the River Drance (and so the current topography reflects relief disruption rather than the situation before the flood), and in the 1950s, the construction of the Mauvoisin dam was accompanied by the building of hydraulic power facilities and water retention basins in Fionnay. These changes in infrastructure are likely the main cause of this local discrepancy.
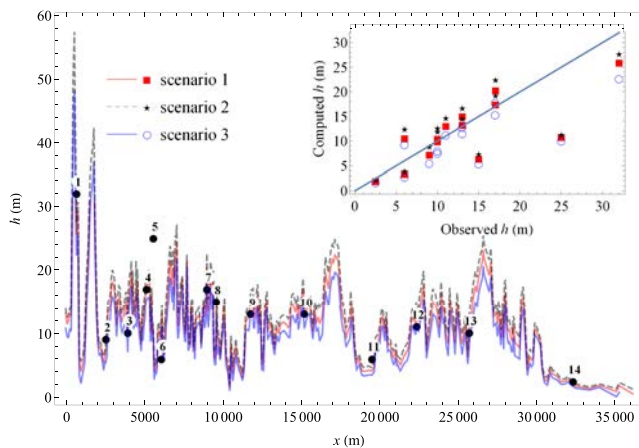
Figure 7. Longitudinal profile of the maximum flow depths for the three scenarios. The black dots show the flow-depth estimates deduced from historical evidence: (1) pont de Mauvoisin, (2) Bonatchiesse, (3) Brecholay, (4) Fionnay, (5) Fionnay gorges, (6) Plamproz, (7) Lourtier, (8) Morgnes, (9) Champsec, (10) Le Châble, (11) Sembrancher, (12) Les Trappistes, (13) Bovernier, and (14) Martigny. For the individual flow-depth profiles and further information (see Text S19). The inset shows the comparison between the computed and observed flow depth for each scenario.

In the supporting information (and data repository), we provide maps comparing the maximum flow depth with the historical information (see Figures S28 to S31). In the data repository, we provide the corresponding georeferenced raster files.

5. Discussion

5.1. Comparison With Other Outburst Floods

A number of studies have looked at the correlation between a flood's peak discharge Q_p and its drained volume. In most cases, Q_p was estimated from geomorphological data. By examining 10 documented events, Clague and Mathews (1973) found that the peak discharge Q_p was indeed correlated with drained volume V: $Q_p \propto V^b$ with $b = 2/3$. Using 72 documented events of glacial lake outburst floods, Walder and Costa (1996) discovered that tunnel draining was the most common form of failure (90% of occurrences) and that peak discharges closely followed the Clague-Mathews empirical equation:

$$Q_p = 0.005V^{0.66}, \tag{5}$$

with $V \times 10^6$ in cubic meters and Q_p in cubic meters per second. This peak discharge equation yields much lower values than those observed from landslide-dammed lakes (see Figure 8). When tunnel draining was not the cause of failure, Walder and Costa (1996) obtained a correlation that was closer to that of landslide-dammed lakes:

$$Q_p = 2.51V^{0.44}. \tag{6}$$

With $Q_p \sim 14{,}500$ m³/s and $V \sim 16.5 \times 10^6$ m³, the Giétro flood was among the most intense floods documented (relative to its volume) regardless of the dam material. For ice dams, the Giétro flood's peak discharge is among the highest values.

5.2. Relevance of the Computational Framework

The core assumption underlying the approach presented in this paper is that we can focus on the water flow without paying particular attention to the details such as bed scouring and sediment transport. This does not mean that these details are unimportant but that their effects do not modify the physics of the broader flow.

This core assumption makes sense when working on large spatial scales: For the Giétro flood simulations of the Drance Valley (see Figure 1), the length of the computational domain exceeds 40 km, and water flow is the main process over such distances. Neglecting a certain level of detail has many advantages. First, any scientific approach should always start with the simplest possible model as this can be refined whenever necessary. Second, taking additional processes into account adds uncertainty, sometimes to the point of introducing noise rather than pertinent information into the computations. Even in the case of controlled experiments, under steady-state flow conditions and a constant sediment feed rate, bedload transport rates show considerable scatter, and therefore, bedload transport equations are only accurate to within a factor of 5 (Dhont & Ancey, 2018). It comes as no surprise that discrepancies are more significant when these equations are compared with field data (Recking et al., 2012). It is difficult to determine whether the current lack of accuracy in sediment transport models will be exacerbated or alleviated when looking at sediment transport associated with megafloods. Third, our idea was to create a model using the lowest possible number of parameters, preferably physical parameters that could be estimated independently of the field data rather than parameters which would require calibration. In this way, all or part of the historical field data serves to test the reliability of the computational model. Although there is clear evidence of intense sediment transport, we have no direct way of estimating the sediment transport rates or delineating aggradation and degradation zones from the existing field data. Any reconstruction of the part played by sediment transport in the 1818 flood is thus highly speculative.
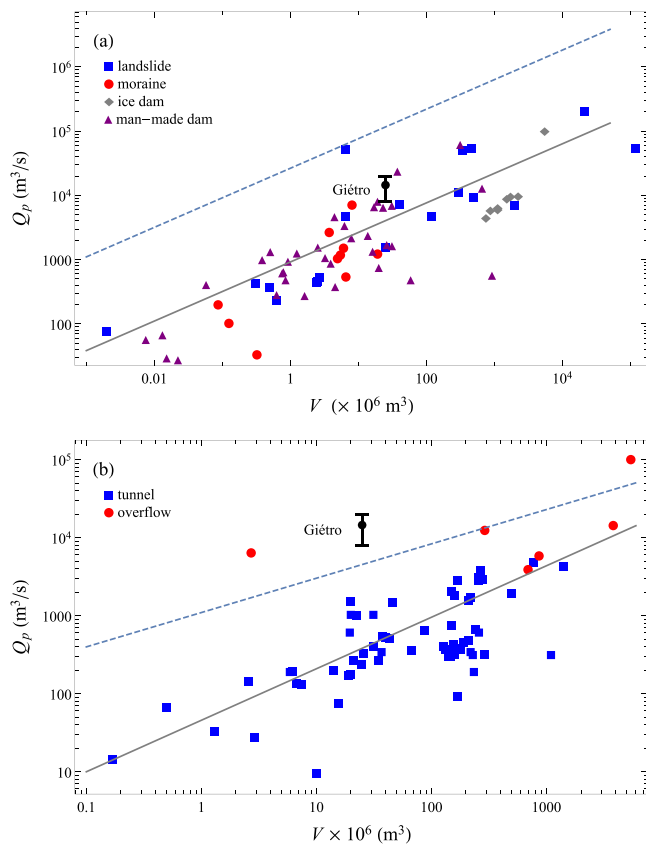
Figure 8. (a) Relationship between drained volume V and peak discharge Q_p, depending on the type of dam. The regression curve $Q_p = 1.6V^{0.46}$ (solid line) shows the mean trend, whereas the envelope $Q_p = 46V^{0.46}$ (dashed line) shows the upper bound. (b) Relationship between drained volume V and peak discharge Q_p, depending on the rupture mode. The solid line represents equation (5), whereas the dashed line represents equation (6). We have also plotted the possible range of the 1818 Giétro flood's peak discharge. Data and equations taken from Walder and Costa (1996) and Walder and O'Connor (1997).

Let us read through the main assumptions and findings of our computational framework before discussing the consistency of result. The framework involves two steps: hydrograph computation (prefailure phase) and flood routing (postfailure phase). Based on descriptions made by Escher von der Linth and other witnesses, we consider a two-stage prefailure phase. In the earliest moments of the drainage, the outflow rate was essentially controlled by thermodynamics: The heat convected by the water flow in the tunnel caused the tunnel's ice walls to melt. The model's parameters are lake temperature T_l, tunnel slope i, ice roughness k_s, and incision rate parameter Γ. The potential ranges of these parameters are narrow, and among them, lake temperature and tunnel slope are the most influential. As shown in Figure 4b, the model provides a drainage phase description consistent with Escher von der Linth's data (in Table 2). Toward the end of the drainage, the outflow rate was controlled by the breach's geometry, which changed suddenly and substantially as a result of ground scouring at the dam's foot (a cantilever failure was probably the final cause of the ice dam's failure). The only historical information available is that it took 30 to 35 min to empty the lake whose volume Escher von der Linth estimated at 18×10^6 m³ (by digitizing the elevation contour lines, we estimated that volume to be 16.4×10^6 m³). To model the fast-drainage stage, we consider that the ice dam behaved like a breached weir and thus the incision rate is given by a mechanical erosion rate e, which is purely empirical (i.e., there is no physics behind it). This parameter was fitted with the drainage duration of close to 30 min. The hydrograph's shape and duration depend crucially on e: the lower e, the lower the peak discharge and the more gradual the hydrograph's rising limb, as shown by Figure 4. Yet, although the initial hydrograph has a significant influence on flood dynamics over short periods ($t < 10$–15 min), its influence wanes over longer ones ($t > 15$ min). As shown in Figures 5 and 7, the differences between scenarios are lower, whereas the peak discharge increases from 9,000 (Scenario 2) to 17,500 m³/s (Scenario 3) when e is increased by 100, from 5×10^{-4} to 0.05 s/m. The inset of Figure 7 does not show any substantial differences between the scenarios' computed flow depths.

For flood routing, we used the numerical Iber code to solve the shallow-water equations. The main parameter was the Manning friction factor n. To match the computed front position and the historical data, we took $n = 0.08$ s/m$^{1/3}$. Although this value is not unrealistic—it is typical of shallow flows on coarse beds, for instance, mountain streams (Bonetti et al., 2017)—it is high. This point is discussed in the next subsection. Assuming a constant n value throughout the computational domain, we were able to capture the time variations in the flood's front position x_f (see Figure 5), and comparing computed and observed maximum depth profiles shows an overall agreement (see Figure 7). As the Manning friction coefficient n is expected to vary spatially (depending on bed structures and their relative submergence) and temporally (as the flow depth changes with time; García, 2007), the question arises as to whether the assumption of constant n for the entire flood body leads to significant errors in the flow-depth computations. Sensitivity tests did not show a great dependence of flow depth on the Manning coefficient n, and furthermore, the different scenarios considered here lead to a fairly good agreement with the observations. We thus conclude that the assumption of constant n is not a critical one. A related question is whether the shallow-water equations are well suited to deal with dam-break flows that experience substantial three-dimensional effects (for instance, because of the valley narrowings and widenings). Horna Munoz and Constantinescu (2018) conducted a comparison between the shallow-water equations and three-dimensional Reynolds-averaged Navier-Stokes equations and found differences of about 10% in the computed hydrographs along the Iowa River. As this
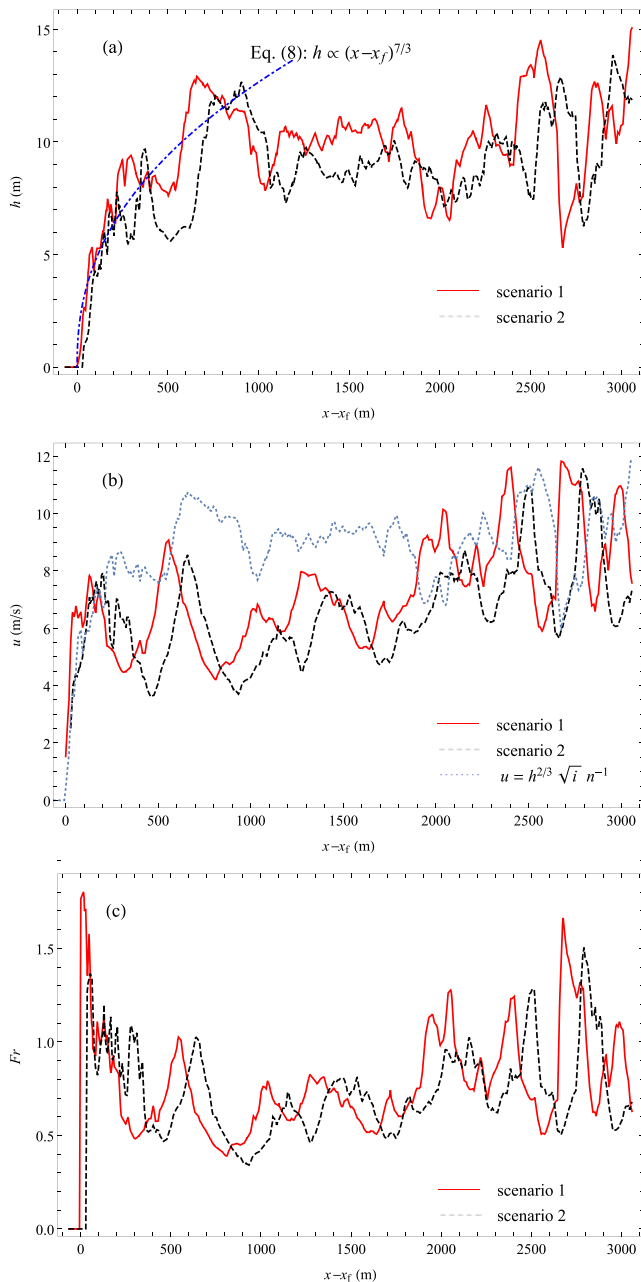
Figure 9. Longitudinal profiles of (a) the flow depth, (b) velocity, and (c) Froude number for Scenarios 1 (red solid line) and 3 (blue dashed line). In (a), the dot-and-dash line shows the flow depth profile equation (8), and the dotted line in (b) shows the steady-state velocity, that is, the depth-averaged velocity that a flow with the same flow depth would reach if it were steady and uniform (for Scenario 1).

value is below the uncertainty range in our computations, we conclude that the errors made in neglecting three-dimensional effects are consistent with our general computational framework.

5.3. Flow Resistance

Flow resistance arises from inner energy dissipation (due to turbulence) and dissipation induced by bed topography. With flow depths as large as 20 m, we would expect low n values. We ran simulations for n ranging from 0.04 (smooth) to 0.15 s/m$^{1/3}$ (very rough). We found that the front moved at a fairly constant velocity, which varied with n as $\bar{u}_f = 2.89/n^{1/3}$ (see Text S13). Local deviations from this linear trend can be observed, with the local front velocity exhibiting a more pronounced dependence on n. For instance, at Le Châble, the front velocity varies as $u_f \propto 1.55/n^{0.58}$. Values as high as 0.08 to 0.12 s/m$^{1/3}$ are required for the computed front position to match the recorded values (see the supporting information for the sensitivity tests).

Several processes explain this higher n value. First, the flood involved intense sediment transport even though our computations ignore it. In the early moments of the dam failure, it is highly likely that the sediment transport took the form of debris flows, and locally, the flood undermined the base of several slopes, causing landslides in numerous places. According to witnesses, the flood also transported large volumes of woody and rocky debris. Sediment transport increases energy dissipation, which is reflected by a higher n value. Some authors have used the Manning equation for modeling the bottom shear stress of debris flows (even though the rheology of debris mixtures is more complicated than that of water and so the bottom shear stress departs substantially from the Manning equation), and they obtained values of n close to 0.1 s/m$^{1/3}$ (Rickenmann, 1999). For floods involving woody debris, Dudley et al. (1998) found n values as high as 0.2 s/m$^{1/3}$. Similarly, dam-break waves traveling through dense vegetation experience high resistance: For instance, Melis et al. (2019) found $n = 0.05$ s/m$^{1/3}$ in their experiments. The value $n = 0.08$ s/m$^{1/3}$ used here confirms the significance of sediment and debris transport in the flow dynamics.

One striking feature of Figure 5 is that the instantaneous front velocity $\dot{x}_f$ reaches similar values regardless of the scenario considered. Although the initial hydrograph (duration and peak discharge) influences early flood motion, it has little effect on the front position after longer periods. This result suggests that the front plays a specific role, which will be analyzed in the next subsection.

5.4. Leading Edge's Dynamics

Figure 9 shows the depth, velocity, and Froude number profiles when the flood front reaches Le Châble ($x_f = 13,500$ m) in Scenarios 1 and 3. Remarkably, the profiles look similar, whereas the initial peak discharges varied by a factor of 1.5 (from $Q_p = 9,000$ to $14,500$ m^3/s), and the initial rising limb was much steeper in Scenario 1 than in Scenario 3. The flow depth rapidly increases from 0 to 10 m within the leading edge—the first 500 m behind the front x_f—then fluctuates wildly around the plateau value of 10 m. Most fluctuations are driven by changes in the cross sections. The velocity within the leading edge is about 6 m/s and it increases, while experiencing large fluctuations, as one measures further toward the flood tail. The leading edge reaches a supercritical regime, while part of the flow behind it is in a subcritical regime marked by a few transitions to the supercritical regime. Figure 9 suggests that the leading edge behaves like a plug pushed by the flow (i.e., with little apparent deformation in the absence of velocity and depth variations). Because of the substantial flow

resistance experienced by the front, its velocity is lower than the tail's velocity. Figure 9 compares the computed and steady-state velocities: Behind the front, over a distance of 2 km, the computed velocity is lower than the steady-state velocity $\sqrt{i}h^{2/3}/n$ (with i bed slope), whereas for $x_f - x > 2$ km, the two velocities are comparable. The flow thus has to deal with the front's braking action. One can wonder whether this "plus effect" is realistic or merely incidental. The Giétro flood's witnesses described an accumulation of debris near the front, which was likely to produce just such a plug effect. Although evidence is sparse, experiments have confirmed the formation of a coarse-particle-rich leading edge, which modifies the flow dynamics, when a dam-break wave erodes the bed (Capart & Young, 1998; Fraccarollo & Capart, 2002; Spinewine & Zech, 2007).

We can gain more physical insights into the leading edge's behavior, however. Assuming that inertia is negligible and that the leading edge's dynamics are dictated by the dominant balance between the pressure gradient and bottom shear stress (Ancey et al., 2008; Dressler, 1952), we get

$$\varrho g h \frac{\partial h}{\partial x} = \varrho g n^2 \frac{u^2}{h^{1/3}}, \tag{7}$$

and assuming that the velocity is constant within the leading edge ($u = \dot{x}_f$) and fixed by the front velocity $\dot{x}_f$, we deduce the flow depth profile by integrating equation (7)

$$h = \left(\frac{7}{3} n^2 \dot{x}_f^2 (x_f - x) \right)^{7/3}. \tag{8}$$

This shows that the leading edge behavior is close to that of a traveling wave. Indeed, writing $x_f = ct + a$ where a is constant and $c = \dot{x}_f$, the flow depth equation (8) takes the form $f(x - ct)$ typical of traveling waves. As shown by Figure 9, the approximate flow depth profile equation (8) captures the numerical data. Remarkably, this equation also captures the flow depth profile after the flood has traveled several kilometers down the River Drance.

6. Conclusion

In this paper, we have presented a reconstruction of the 1818 Giétro outburst flood. The core assumption was that, as a first approximation, we could focus on water flow and ignore bed erosion, deposition, and sediment transport. The computational framework involved two steps: lake drainage and flood routing. First, to compute the initial hydrograph, we considered the lake's mass balance. The outflow rates were estimated by assuming that the tunnel drilled through the ice dam by Venetz, the Cantonal Engineer, behaved like a broad-crested weir. Because the ice-tunnel walls gradually melted, its dimensions increased throughout the slow drainage phase. Eventually, the ice dam failed, causing fast drainage of the lake's remaining water volume. Second, we solved the shallow-water equations numerically to model the ensuing flood (using the academic Iber code).

The computational framework involved six adjustable parameters: four for the slow drainage phase (lake temperature T_l, tunnel slope i, ice roughness k_s, and the incision rate parameter Γ), one for the fast-drainage phase (mechanical erosion rate e), and one for the flood routing (Manning coefficient n). These parameters were adjusted using field data (water level z_l for the slow drainage phase, failure duration for the fast drainage phase, and front position x_f over time for flood routing). Note that all but one of these parameters were physically constrained to lie within a narrow range of possible values, so the parameter adjustments were not a fitting exercise. We used other field data to assess the model's performance (shape of the $z_l(t)$ curve, dimensions of the breach, flow-depth profile, and flooded area). We found that the computational framework successfully captured almost all the available historical information. The only noticeable discrepancy was the maximum flow depth in the village of Fionnay, but the topography around this hamlet has substantially changed since the early nineteenth century.

The numerical analysis led to the following estimates for the 1818 Giétro flood: maximum lake volume 27×10^6 m^3, water volume drained during the fast-drainage phase 18×10^6 m^3, peak discharge $Q_p = 14,500$ m^3/s, and mean front velocity 5 to 6 m/s. As shown by Figure 8, the 1818 Giétro flood ranks among the most intense recorded floods for this range of volume, regardless of the failure scenario.

There is historical evidence that the outburst flood was associated with debris flows, landslides, and sediment transport. Although we did not account for these phenomena explicitly, we implicitly incorporated their effects on flood dynamics by setting a high value for the Manning friction coefficient: $n = 0.08 \text{ s/m}^{1/3}$. High flow resistance caused the flood's leading edge to behave like a plug. The flood body pushed the leading edge but also had to deal with the lower velocities within the flood's leading edge. Strikingly, the leading-edge dynamics were weakly sensitive to the flood's features (initial hydrograph and total water volume). This weak sensitivity is the reason why all three of the scenarios considered demonstrated similar features in their leading edges (front's instantaneous velocity and flow depth profile). The Drance Valley has a (narrow) topographical configuration which made it particularly well suited for the flood's leading edge to exhibit plug-like behavior. If the valley had been wider and more open, we presume that debris accumulation in the leading edge would have come to a halt more rapidly and then been bypassed by the flood body.

Apart from its interest to scholars and Switzerland's local authorities, the Giétro flood is a good candidate with which to benchmark hydraulic models. The case is well documented: We have historical information on the initial conditions, front propagation, and damage caused by the flood. From the epistemological standpoint, how Ignaz Venetz coped with the situation and found an astute (albeit imperfect) solution, showed that in the early nineteenth century, people had started to face up to sudden environmental threats and were trying to tame the destructive forces of nature. In contrast, under similar circumstances in 1595, the valley's inhabitants did not try to alleviate the dire potential consequences of the foreseeable flood. The same situation occurred in 1219 when the Oisans Lake's debris dam failed and swept through Grenoble (France), one of the major historical flash floods caused by a dam failure in Europe during the Middle Ages (Berlioz, 1998). By the nineteenth century, floods were no longer perceived to be acts of God but rather a misfortune (Walter, 2008). The Giétro flood is also interesting in terms of its risk management aspects. Not only did local authorities quickly intervene to reduce the threat as of May 1818, but in the aftermath of the disaster, specific measures were implemented to protect populations and avoid new disasters. These efforts were not only local but also became nationwide (Payot & Meilland, 2018a; 2018b).

Appendix A: Filling of the Giétro Lake in the Spring of 1818

Water supply to the lake was estimated using the GERM, which has been devised to compute runoff from glacier-covered watersheds by accounting for snow accumulation distribution, snow and ice melt, glacier geometry change, evapotranspiration, and runoff. A detailed description of the model can be found in Huss et al. (2008).

The model runs on a spatial grid with 50-m resolution at a daily scale and accounts for all types of runoff generation processes in alpine catchments (snow and ice melt, solid/liquid precipitation and snow redistribution, evapotranspiration, runoff routing, and glacier advance and retreat). The catchment (105 km^2) was roughly 50% glacierized around the Year 1818. The glacier extent at that time was retrieved from historical maps. Time series (including monthly average air temperature and precipitation totals continuously from 1817 on) are available from the Grand-St-Bernard station (2,478 m asl). At a distance of 20 km and an elevation similar to the study site, this station is considered suitable to model drainage basin runoff. As the model requires a daily meteorological forcing, we have generated five distinct daily series of temperature and precipitation by superimposing observed day-to-day variations of randomly chosen years drawn from the daily records at Grand-St-Bernard (available since 1865) on the monthly observations of the hydrological Years 1817/1818 to 1819/1820. In the absence of both catchment runoff measurements and data on glacier mass change in the early nineteenth century, an unambiguous calibration of the glacio-hydrological model is difficult. Model parameters prescribing snow accumulation and snow/ice melting are chosen such that the resulting values of winter and annual glacier mass balance are within realistic ranges, inferred from modern mass-balance observations of glaciers in the Mauvoisin basin, for the given period. Three equally reasonable parameter sets were chosen, and the model was run with every parameter set; each set used the five possible realizations of daily meteorological forcing. Our best estimate of daily runoff's contribution to the glacial lake was obtained by averaging the 15 model runs. The meteorological forcing used and the daily runoff series are provided in the supporting information in a file called "GERM data." These data cover the Hydrological Years 1817–1818 to 1819–1820, allowing a comparison between the spring of 1818 (lake drainage event) and the next year.

A power law function was fitted to the GERM data for the month of June 1818:

$$V(t) = \begin{cases} 0 \text{ for } t < t_i, \\ V_0(t/t_0)^n \text{ for } t \geq t_i, \end{cases} \tag{A1}$$

where $V(t)$ is the water volume supplied to the lake (in m^3), $n = 2$ is an exponent, t_i is the inception date arbitrarily set at Monday, 18 May (in s), t_0 is the time at which the lake drained (16 June 1818, 10 p.m.), and V_0 an estimate of the lake volume at that time (29×10^6 m^3). The parameters were adjusted by trial and error. Figure S8 compares the GERM data and the empirical fit.

From the volume $V(t)$, we infer the incoming flow rate (see also Figure S7)

$$Q_{in}(t) = \dot{V}(t). \tag{A2}$$

We digitalized the Siegfried map' contour lines in the area including the lake. For each elevation of the lake's free surface z_l, we computed the corresponding volume lake (see Figure S8). Finally, we fitted a sixth-order polynomial to these volumes

$$V(z_l) = \sum_{i=0}^{6} a_i z_l^i, \tag{A3}$$

with $a_0 = -5.38857 \times 10^{13}$, $a_0 = 1.14943 \times 10^{11}$, $a_2 = -7.60577 \times 10^7$, $a_3 = -1,096.58$, $a_4 = 22.5825$, $a_5 = -0.00954752$, and $a_6 = 1.26879 \times 10^{-6}$. From this relationship, we deduced the lake's free-surface area $A(z_l)$

$$A(z_l) = V'(z_l), \tag{A4}$$

as a function of the free-surface elevation z_l.

Appendix B: Derivation of the Governing Equations

B.1. Outgoing Flow Rate

We assume that when entering the tunnel, the water flow had a free surface over the entire length of the tunnel. Pressure-driven phases (for instance, due to free-surface instabilities, ice chunks jamming the tunnel, and wall collapse) were possible, especially at early times, but they are ignored. We also assume that the flow in the tunnel was supercritical, with no influence of the downstream condition on the flow. See Figure B1 for a sketch of the geometry considered in the paper and the notation associated.

The outgoing water flow rate Q_{out} is controlled by a number of parameters: the tunnel width w_s, its length L, the lake depth z_l, its width W, the entrance curvature r, and the mean angle γ of the flow upstream of the tunnel (the list of parameters is not complete). A common assumption is that the flow depth reaches the critical value $h_c = \sqrt[3]{q_o^2/g}$ at Point B, where $q_o = Q_{out}/w_s$. In other words, the ice dam behaves like a perfect weir. The Bernoulli equation applied to the AB streamline then gives $h_c = 2\Delta z/3$, with $\Delta z = z_l - z_s$. We thus get

$$Q_{out} = \left(\frac{2}{3}\right)^{3/2} w_s \sqrt{g\Delta z^3}. \tag{B1}$$
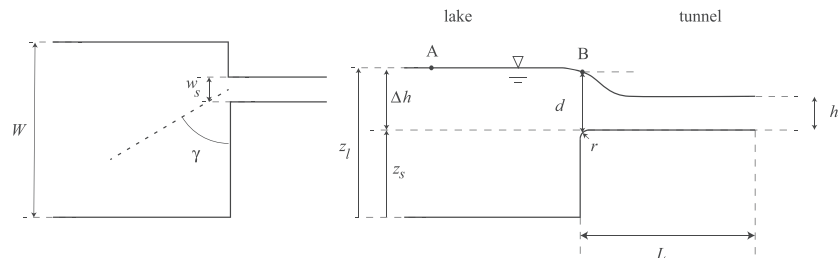

Figure B1. Sketch and notation. (left) View from above of the lake and tunnel. (right) Flow past a rounded broad-crested weir.

In practice, this expression provides the upper bound of the water discharge. An empirical discharge coefficient c_d is introduced to account for the various physical processes that reduce flow rate (Hager, 2010)

$$Q_{out} = c_d \left(\frac{2}{3}\right)^{3/2} w_s \sqrt{g\Delta z^3}, \tag{B2}$$

where c_d depends on the width ratio $\psi = w_s/W$, the length ratios $\lambda = L/w_s$ and $\xi = \Delta z/L$, the curvature $\varsigma = r/z_s$, and the angle γ. Analytical and approximate expressions have been obtained in end-member cases. For $\lambda \to \infty$, $\psi \to 0$, and $z_s = 0$, Hager and Dupraz (1985) obtained $c_d = 0.715$. For square long-crested weirs ($\lambda \to \infty$ and $\varsigma \to 0$), Moss (1972) obtained $c_d = 0.87$. For broad-crested weirs, Hager and Schwalt (1994) proposed the empirical relationship (see Figure S9)

$$c_d = \frac{c_{d0}}{1-\phi}\left(1 - \frac{\phi}{1+\xi^4}\right), \tag{B3}$$

with $\phi = 2/9$ and $c_{d0} = 0.846$. Hager (2010) extended this relation to narrowing and rounded weirs

$$c_d = \frac{c_{d0}c_b c_r}{1-\phi}\left(1 - \frac{\phi}{1+\xi^4}\right) \text{ with } c_b = 1 - \frac{8}{60(1+\xi^4)} \text{ and } c_r = 1 + 0.1\sqrt{3\varsigma}\exp(1-3\varsigma), \tag{B4}$$

with c_b reflecting width reduction (holding for $0.25 \leq w_s/W \leq 0.75$) and c_r inlet rounding.

Applying the Bernoulli equation to the AB streamline segment and using a Borda-like head loss $\Delta H = \zeta \bar{u}^2/(2g)$ ($\bar{u}$ depth-averaged velocity, $\zeta = 1/2$) as an approximation of the energy dissipation and flow contraction at the tunnel entrance, we can express the total head

$$H = z_l = z_s + h_c + \frac{1}{2g}\left(\frac{Q_0}{h_c w_s}\right)^2 (1+\zeta),$$

from which we deduce

$$Q_{out} = \left(\frac{4}{7}\right)^{3/2} w_s \sqrt{g\Delta z^3}, \tag{B5}$$

or, in other words, $c_d = (6/7)^{3/2} = 0.79$.

We can consider that initially, the water flow experienced substantial energy dissipation due to flow contraction. Values of c_d as low as 0.70 seem reasonable. When the flow started incising and widening the tunnel, this dissipation decreased gradually, causing c_d to increase. Values close to 0.9 seem realistic. In the following, we will simply assume that c_d is constant: $c_d = 0.7$.

B.2. Mass Conservation for the Lake
For the lake, mass conservation implies

$$A(z_l)\frac{dz_l}{dt} = Q_{in} - Q_{out}, \tag{B6}$$

where the incoming flow rate Q_{in} is given by equation (A2) and the outgoing discharge Q_{out} is given by equation (B2) with $c_d = 0.7$.

B.3. Momentum Conservation for the Water Flow
We assume that the flow section remained rectangular, with its width denoted by w_s and its flow depth by h. The tunnel slope is denoted by i. Wall friction can be described using the Darcy-Weisbach relation

$$\tau = \varrho f \frac{1}{8}\bar{u}^2,$$

with f the Darcy-Weisbach friction factor and $\bar{u}$ the depth-averaged velocity. Here we prefer Darcy-Weisbach over the Manning law because ice walls are smooth and the water velocity high ($\bar{u}$ is expected to be higher than 10 m/s). The glaciology community seems to prefer Manning, however, as Manning friction is constant regardless of the flow depth relative to the roughness (Clarke, 2003). In hydraulics, the Darcy-Weisbach is often considered more physical (Yen, 2002).

Many empirical equations have been proposed to make the classic Colebrook-White (relating f to the flow properties) explicit. For instance, Yen (2002) suggested

$$f = \frac{1}{4}\left[-\log_{10}\left(\frac{1}{12}\frac{k_s}{R_h} + \frac{1.95}{Re^{0.9}}\right)\right]^{-2}, \tag{B7}$$

holding for $k_s/R_h < 0.05$ and $Re > 30 \times 10^3$. The Reynolds number is defined as

$$Re = \frac{\bar{u}R_h}{\nu}, \tag{B8}$$

where $R_h = w_s h/(w_s + 2h)$ is the hydraulic radius. The roughness size is denoted by k_s.

As the initial tunnel length was long (about 200 m) and the flow was supercritical, the flow quickly reached its normal depth h_n. That depth is found by solving the steady-state equation for uniform flow

$$\tau = \varrho f \frac{1}{8}\bar{u}^2 = \varrho g R_h i. \tag{B9}$$

There are analytical solutions to this equation when f is constant. We can also build approximate solutions in the following way. Reworking equation (B9), we get

$$Q^2 = \frac{8g}{f}i^2\frac{w_s^3 h^3}{\chi}, \tag{B10}$$

with $Q = \bar{u}w_s h$ the flow rate. Setting

$$K = \frac{f}{8i}\frac{Q^2}{w_s^5 g} \text{ and } \varsigma = \frac{h}{w_s},$$

then equation (B10) is equivalent to the dimensionless equation

$$K = \frac{\varsigma^3}{1 + 2\varsigma}. \tag{B11}$$

Although this third-order polynomial has closed-form solutions, it is interesting (numerically) to fit a power law function to the solution (see Figure S10)

$$\varsigma = 1.62K^{0.45} \Rightarrow h_n = 1.62\left(\frac{f}{8i}\frac{Q^2}{w_s^5 g}\right)^{0.45}w_s. \tag{B12}$$

B.4. Energy Conservation for the Water Flow Along the Tunnel

In the tunnel, applying energy conservation to a flow slice gives

$$\varrho w_s h\frac{d\varepsilon}{dt} = \tau\chi\bar{u} - q\chi, \tag{B13}$$

where ε is the internal energy (per unit mass), the derivative is the material derivative, τ is the bottom shear stress, $\chi = 2h + w_s$ is the wetted perimeter, q is the heat flux, $\bar{u}$ is the depth-averaged velocity, and h the flow depth. Here, for isochoric flows, we have $d\varepsilon = c_w dT$ with c_w the specific heat of water.

The heat flux is given by

$$q = \hbar\Delta T, \tag{B14}$$

where $\hbar$ is the heat transfer function and $\Delta T = T - T_i$ is the temperature difference between flowing water (T) and ice (T_i). The heat transfer function is mostly expressed using the Nusselt number Nu when heat flux is driven by forced convection

$$\hbar = \frac{k_w}{L_*}N_u,$$

where L_* is a characteristic length and k_w is the thermal conductivity of water. In glaciology, the Dittus-Boelter equation is often used (and preferred over other more complicated empirical laws) to define

the dependence of the Nusselt number on the problem variables for turbulent flows in smooth conduits of diameter D and length ℓ: we set $L_* = D$. This equation writes

$$N_u = 0.023 Re^{4/5} Pr^n, \tag{B15}$$

with $Re = L_* \bar{u}/\nu$ the Reynolds number (with n the kinematic viscosity), $Pr = \varrho \nu c_p / k_w$ the Prandtl number (c_p specific heat), and n a parameter ($n = 0.3$ for a cooling fluid and $n = 0.4$ for a heating fluid; Bergman et al., 2011). The equation holds for $\ell / D > 10$ and $Re > 10^4$. For noncylindrical conduits, in this case a channel, the diameter is replaced with the hydraulic diameter $D_{\text{h}} = 4R_h = 4w_s h/(w_s + 2h)$. The empirical Dittus-Boelter law suffers from inaccuracies: Uncertainties as large as 25% are reported (Bergman et al., 2011).

An alternative to the Dittus-Boelter equation is the Gnielinski equation, which provides more accurate estimates of N_u and holds for a wider range of the Reynolds number

$$N_u = \frac{f}{8} \frac{Pr(Re - 1,000)}{1 + 12.7\sqrt{f/8}(Pr^{2/3} - 1)}, \tag{B16}$$

with f the Darcy-Weisbach friction factor (Bergman et al., 2011). This equation is valid for $Re > 3,000$. As it depends on f, the Gnielinski equation may give significantly different results from those yielded by the Dittus-Boelter equation (see Figure S11).

In the end, the heat flux writes

$$q = k_w N_u \frac{\Delta T}{D_{\text{h}}}, \tag{B17}$$

and the energy equation (B13) becomes

$$\varrho w_s h c_w \left(\frac{\partial T}{\partial t} + \bar{u} \frac{\partial T}{\partial x} \right) = \chi \left(\tau \bar{u} - k_w N_u \frac{\Delta T}{D_{\text{h}}} \right), \tag{B18}$$

The orders of magnitude of the different terms make it possible to appreciate the part played by each process. We consider that $Q = O(100)$ m³/s, $\bar{u} = O(10)$ m/s, $w_s = O(10)$ m, $h = O(1)$ m, $L = O(200)$ m, $T = O(1)$ K, and $i = 1\%$. The second term on the left-hand side (called the *dissipation function*) is

$$\varrho w_s h c_w \bar{u} \frac{\partial T}{\partial x} \sim 2.1 \times 10^6 \text{W/m}.$$

The first term on the right-hand side is

$$\chi \tau \bar{u} = \varrho g Q i \sim 10^4 \text{W/m},$$

while the second term is

$$\chi k_w N_u \frac{\Delta T}{D_{\text{h}}} \sim 71 \text{W/m}.$$

All the energy used to melt ice stems from the internal energy of flowing water, and over a distance of 200 m, the temperature decrease should be limited to a few percent (here 3% with the values considered above; see Figure S12). The ice can be assumed to be temperate, and thus, no heat conduction occurs through the ice wall. The energy balance for the state change is

$$\chi q = \varrho_i (-w_s \dot{z}_s + h \dot{w}_s) L, \tag{B19}$$

where L is the latent heat.

To close this equation, we need to specify how the vertical and lateral incision rates are related. In prismatic channels, the sidewall shear stress τ_w is lower than the bottom shear stress τ_b (Guo & Julien, 2005; see Figure S13). Melting does not occur homogeneously through the ice layer. Part of the layer weakened by the melting is eroded by the flowing water, and this is even more likely as the shear stress is high. We define an empirical incision rate factor Γ

$$\dot{w}_s = -\Gamma \dot{z}_s. \tag{B20}$$

We expect $\Gamma < 1$ (the vertical incision rate is higher than the lateral one), and if the contrast in the incision rate were controlled by the shear stress distribution, then we would have $\Gamma \sim 2/3$.

With this assumption, we can now transform (B19) into an equation that dictates the incision rate of the tunnel bottom

$$\dot{z}_s = -\frac{\chi q}{\varrho_i(w_s + h\Gamma)L}.$$ (B21)

B.5. Failure Phase

In his contemporary account of the flood, Escher von der Linth explained that the cascade at the tunnel outlet caused erosion at the foot of the ice dam. The tunnel length reduced gradually. He wrote that 64.5 hr after the drainage began, there was a rapid drainage phase. We assume that the spillway failure resulted primarily from the rapid mechanical erosion of the spillway. We replace the thermodynamically controlled incision equation (B21) with

$$\dot{z}_s = -e\bar{u}^2,$$ (B22)

where e is an empirical erosion factor. We still assume that the lateral incision rate is given by (B20).

B.6. Final Drainage Phase

When the spillway is eroded to its bottom (at elevation $z_{\text{base}} = 1,800$ m), we assume that the water drains through the trench in the ice dam. We use the same governing equation as before except that there is no longer any vertical incision. Lateral incision is assumed to be zero.

References

ASSHS (2014). *Dictionnaire Historique de la Suisse (online)*. French, German, Italian: Académie suisse des sciences humaines et sociales (ASSHS). http://www.hls-dhs-dss.ch/(ASSHS)

Ancey, C., Iverson, R., Rentschler, M., & Denlinger, R. P. (2008). An exact solution for ideal dam-break floods on steep slopes. *Water Resources Research*, *44*, W01430. https://doi.org/10.1029/2007WR006353

Balmer, H. (1970). Ignaz Venetz 1788–1859. *Gesnerus (Swiss Journal of the History of Medicine and Sciences)*, *27*, 138–168.

Begam, S., Sen, D., & Dey, S. (2018). Moraine dam breach and glacial lake outburst flood generation by physical and numerical models. *Journal of Hydrology*, *563*, 694–710.

Bergman, T. L., Incropera, F., DeWitt, D. P., & Lavine, A. S. (2011). *Fundamentals of heat and mass transfer* (7th). New York: John Wiley.

Berlioz, J. (1998). *Catastrophes naturelles et calamités au Moyen-âge*. Florence: Sismel Edizioni del Galluzzo.

Bladé, E., Cea, L., Corestein, G., Escolano, E., Puertas, J., Váquez-Cendón, E., et al. (2014). Iber: Herramienta de simulación numérica del flujo en ríos. *Revista Internacional de Métodos Numéricos para Cálculo y Diseño en Ingenieria*, *30*, 1–10.

Bohorquez, P., & Darby, S. (2008). The use of one- and two-dimensional hydraulic modelling to reconstruct a glacial outburst flood in a steep Alpine valley. *Journal of Hydrology*, *361*, 240–261.

Bonetti, S., Manoli, G., Manes, C., Porporato, A., & Katul, G. G. (2017). Manning's formula and Strickler's scaling explained by a co-spectral budget model. *Journal of Fluid Mechanics*, *812*, 1189–1212.

Capart, H. (2013). Analytical solutions for gradual dam breaching and downstream river flooding. *Water Resources Research*, *49*, 1968–1987. https://doi.org/10.1002/wrcr.20167

Capart, H., Spinewine, B., Young, D., Zech, Y., Brooks, G. R., Leclerc, M., & Secretan, Y. (2007). The 1996 Lake Ha! Ha! breakout flood, Québec: Test data for geomorphic flood routing methods. *Journal of Hydraulic Research*, *45*, 97–109.

Capart, H., & Young, D. (1998). Formation of a jump by the dam-break wave over a granular bed. *Journal of Fluid Mechanics*, *372*, 121–135.

Carrivick, J. (2010). Dam break—Outburst flood propagation and transient hydraulics: A geosciences perspective. *Journal of Hydrology*, *380*, 338–355.

Carrivick, J., & Tweed, F. (2016). A global assessment of the societal impacts of glacier outburst floods. *Global and Planetary Change*, *144*, 1–16.

Carrivick, J. L., Tweed, F. S., Ng, F., Quincey, D., Mallalieu, J., Ingeman-Nielsen, T., et al. (2017). Ice-dammed lake drainage evolution at Russell Glacier, West Greenland. *Frontiers in Earth Science*, *5*, 100.

Castro-Orgaz, O., & Hager, W. H. (2013). Unsteady Boussinesq-type flow equations for gradually-eroded beds: Application to dike breaches. *Journal of Hydraulic Research*, *51*, 203–208.

Castro-Orgaz, O., & Hager, W. (2017). *Non-hydrostatic free surface flows*. Berlin: Springer.

Cea, L., & Bladé, E. (2015). A simple and efficient unstructured finite volume scheme for solving the shallow water equations in overland flow applications. *Water Resources Research*, *51*, 5464–5486. https://doi.org/10.1002/2014WR016547

Chanson, H. (2004). *The hydraulics of open channel flow: An introduction* (2nd). Amsterdam: Elsevier Butterworth Heinemann.

Chow, V. (1959). Open-channel hydraulics.

Clague, J. J., & Mathews, W. (1973). The magnitude of jökulhlaups. *Journal of Glaciology*, *12*, 501–504.

Clague, J., & O'Connor, J. E. (2015). Glacier-related outburst floods. In W. Haeberli, C. D. Whiteman, & J. Schroder (Eds.), *Snow and ice-related hazards, risks and disasters* (pp. 487–523). Amsterdam: Elsevier.

Clarke, G. (1982). Glacier outburst floods from a "Hazard Lake," Yukon Territory, and the problem of flood magnitude prediction. *Journal of Glaciology*, *28*, 3–21.

Clarke, G. (2003). Hydraulics of subglacial outburst floods: New insights from the Spring-Hutter formulation. *Journal of Glaciology*, *49*, 299–313.

Corboz, P. (2015). Reconstitution géohistorique de la débâcle du glacier du Giétro le 16 juin 1818 (Master of Science in Geography), Université de Lausanne.

Costa, J. (1988). Floods from dam failure. In V. Baker, R. Kochel, & P. Patton (Eds.), *Flood geomorphology* (pp. 439–461). New York: Wiley.

Cunge, J. A., Holly, F. M., & Verwey, A. (1980). *Practical aspects of computational river hydraulics*. Boston: Pitman publishing.

Dhont, B., & Ancey, C. (2018). Are bedload transport pulses in gravel-bed rivers created by bar migration or sediment waves? *Geophysical Research Letters*, *45*, 5501–5508.

Dressler, R. (1952). Hydraulic resistance effect upon the dam-break functions. *Journal of Research of the National Institute of Standards*, *49*, 217–225.

Dubuis, P. (1993). Des horloges dans les montagnes: Premières explorations en Valais, XVe-XIXe siècles. *Vallesia: bulletin annuel de la Bibliothèque et des Archives cantonales du Valais, des Musées de Valère et de la Majorie*, 91–108.

Dudley, S. J., Fischenich, J. C., & Abt, S. R. (1998). Effect of woody debris entrapment on flow resistance. *Journal of the American Water Resources Association*, *34*, 1189–1197.

Dussaillant, A., Benito, G., Buytaert, W., Carling, P., Meier, C., & Espinoza, F. (2010). Repeated glacial-lake outburst floods in Patagonia: An increasing hazard? *Natural Hazards*, *54*, 469–481.

El Kadi Abderrezzak, K., Paquier, A., & Gay, B. (2011). One-dimensional numerical modelling of dam-break waves over movable beds: Application to experimental and field cases. *Environmental Fluid Mechanics*, *8*, 169–198.

Emmer, A. (2017). Glacier retreat and glacial lake outburst floods (GLOFs), *Natural Hazard Science*. Oxford: Oxford University Press. https://doi.org/10.1093/acrefore/9780199389407.013.275

Escher von der Linth, H. C. (1818). *Notice sur le val de Bagnes en Bas-Valais et la catastrophe qui en a dévasté le fond en juin 1818*. Genève: J.J. Paschoud Imprimeur-Libraire.

Faeh, R. (2007). Numerical modeling of breach erosion of river embankments. *Journal of Hydraulic Engineering*, *133*, 1000–1009.

Fischer, M., Huss, M., Barboux, C., & Hoelzle, M. (2014). The New Swiss Glacier Inventory SGI2010: Relevance of using high-resolution source data in areas dominated by very small glaciers. *Arctic, Antarctic, and Alpine Research*, *46*, 933–945.

Flowers, G. E., Björnsson, H., Pálsson, F., & Clarke, G. K. (2004). A coupled sheet-conduit mechanism for Jökulhlaup propagation. *Geophysical Research Letters*, *31*, L05401. https://doi.org/10.1029/2003GL019088

Fraccarollo, L., & Capart, H. (2002). Riemann wave description of erosional dam break flows. *Journal of Fluid Mechanics*, *461*, 183–228.

García, M. (2007). Sediment transport and morphodynamics. In M. García (Ed.), *Sedimentation engineering* (Vol. 110, pp. 21–164). Reston: American Society of Civil Engineers. ASCE Manuals and Reports on Engineering Practice.

Gard, J.-M. (1988). *16 juin 1818 – Débâcle du Giétro*. Le Châble, Valais, Switzerland: Musée de Bagnes.

George, D. (2011). Adaptive finite volume methods with well-balanced Riemann solvers for modeling floods in rugged terrain: Application to the Malpasset dam-break flood (France, 1959). *International Journal for Numerical Methods in Fluids*, *66*, 1000–1018.

Guo, J., & Julien, P.-Y. (2005). Shear stress in smooth rectangular open-channel flows. *Journal of Hydraulic Engineering*, *131*, 30–37.

Haeberli, W. (1983). Frequency and characteristics of glacier floods in the Swiss Alps. *Annals of Glaciology*, *4*, 85–90.

Hager, W. H. (2010). *Wastewater hydraulics: Theory and practice*. Berlin: Springer.

Hager, W. H., & Dupraz, P.-A. (1985). Discharge characteristics of local, discontinuous contractions. *Journal of Hydraulic Research*, *23*, 421–433.

Hager, W. H., & Schwalt, M. (1994). Broad-crested weir. *Journal of Irrigation and Drainage Engineering*, *120*, 13–26.

Harrison, S., Kargel, J. S., Huggel, C., Reynolds, J. M., Shugar, D. H., Betts, R. A., et al. (2018). Climate change and the global pattern of moraine-dammed glacial lake outburst floods. *Cryosphere*, *12*, 1195–1209.

Hervouet, J.-M., & Petitjean, A. (1999). Malpasset dam-break revisited with two-dimensional computations. *Journal of Hydraulic Research*, *37*, 777–788.

Holzhauser, H., & Zumbühl, H. (1999). Glacier fluctuations in the Western Swiss and French Alps in the 16th century. *Climatic Change*, *43*, 5–53.

Horna Munoz, D., & Constantinescu, G. (2018). A fully 3-D numerical model to predict flood wave propagation and assess efficiency of flood protection measures. *Advances in Water Resources*, *122*, 148–165.

Huss, M., Farinotti, D., Bauder, A., & Funk, M. (2008). Modelling runoff from highly glacierized alpine drainage basins in a changing climate. *Hydrological Processes*, *22*, 3888–3902.

Huss, M., Voinesco, A., & Hoelzle, M. (2013). Implications of climate change on Glacier de la Plaine Morte, Switzerland. *Geographica Helvetica*, *68*, 227–237.

ICOLD (1998). Dam Break flood analysis—Review and recommendations (Tech. Rep. No. 111). Paris: International Commission on Large Dams.

Kingslake, J., Ng, F., & Sole, A. (2015). Modelling channelized surface drainage of supraglacial lakes. *Journal of Glaciology*, *61*, 185–199.

Lapointe, M., Secretan, Y., Driscoll, S., Bergeron, N., & Leclerc, M. (1998). Response of the Ha! Ha! River to the flood of July 1996 in the Saguenay Region of Quebec: Large-scale avulsion in a glaciated valley. *Water Resources Research*, *34*, 2383–2392. https://doi.org/10.1029/98wr01550

Larocque, L., Imran, J., & Chaudhry, M. (2013). 3D numerical simulation of partial breach dam-break flow using the LES and $k - \epsilon$ turbulence models. *Journal of Hydraulic Research*, *51*, 145–157.

Luterbacher, J., & Pfister, C. (2015). The year without a summer. *Nature Geoscience*, *8*, 246.

Mariétan, I. (1959). La vie et l'oeuvre de l'ingénieur Ignace Venetz, 1788-1859. *Bulletin de la Murithienne*, *76*, 1–51.

Mathieu, J. (2000). *Storia delle Alpi 1500–1900: Ambiente, sviluppo e società*. Bellinzona: Edizioni Casagrande.

Melis, M., Poggi, D., Fasanella, G. O., Cordero, S., & Katul, G. G. (2019). Resistance to flow on a sloping channel covered by dense vegetation following a dam-break. *Water Resources Research*, *55*, 1040–1058. https://doi.org/10.1029/2018wr023889

Moss, W. (1972). Flow separation at the upstream edge of a square-edged broad-crested weir. *Journal of Fluid Mechanics*, *52*, 307–320.

Mulder, T., Zaragosi, S., Jouanneau, J.-M., Bellaiche, G., Guérinaud, S., & Querneau, J. (2009). Deposits related to the failure of the Malpasset Dam in 1959: An analogue for hyperpycnal deposits from jökulhlaups. *Marine Geology*, *260*, 81–89.

Ng, F., & Björnsson, H. (2003). On the Clague-Mathews relation for jökulhlaups. *Journal of Glaciology*, *49*, 161–172.

Nye, J. (1976). Water flow in glaciers: Jökulhlaups, tunnels and veins. *Journal of Glaciology*, *17*, 181–207.

Payot, C., & Meilland, A. (Eds.) (2018a). *Giétro 1818. La véritable histoire Edited by* Payot, C., & Meilland, A. Fribourg: Faim de Siècle.

Payot, C., & Meilland, A. (2018b). *Giétro 1818. Une histoire vraie*. Fribourg: Faim de Siècle.

Petaccia, G., Lai, C., Milazzo, C., & Natale, L. (2016). The collapse of the Sella Zerbino gravity dam. *Engineering Geology*, *211*, 39–49.

Peter, S., Siviglia, A., Nagel, J. B., Marelli, S., Boes, R., Vetsch, D. F., & Sudret, B. (2018). Development of probabilistic dam breach model using Bayesian inference. *Water Resources Research*, *54*, 4376–4400. https://doi.org/10.1029/2017wr021176

Raymond, M., Wegmann, M., & Funk, M. (2003). Inventar gefährlicher Gletscher in der Schweiz (Tech. Rep. No. Mitteilung 182): ETH Zürich, Versuchsanstalt für Wasserbau.

Recking, A., Liébault, F., Peteuil, C., & Jolimet, T. (2012). Testing bedload transport equations with consideration of time scales. *Earth Surface Processes and Landforms*, *37*, 774–789.

Rickenmann, D. (1999). Empirical relationships for debris flows. *Natural Hazards*, *19*, 47–77.

Spinewine, B., & Zech, Y. (2007). Small-scale laboratory dam-break waves on movable beds. *Journal of Hydraulic Research*, *45*, 73–86.

Valiani, A., Caleffi, V., & Zanni, A. (2002). Case study: Malpasset dam-break simulation using a two-dimensional finite volume method. *Journal of Hydraulic Engineering*, *128*, 460–472.

Vatne, G., & Irvine-Fynn, T. (2016). Morphological dynamics of an englacial channel. *Hydrology and Earth System Sciences*, *20*, 2947–2964.

Venetz, I. (1821). Sur les travaux du glacier de Giétroz. *Naturwissenschaftlicher Anzeiger der Allgemeinen Schweizerischen Gesellschaft für die Gesammten Naturwissenschaften*, *5*(11), 82–84. https://doi.org/10.5169/seals-389349

Venetz, I. (1825). Apologie des travaux du glacier de Giètroz, contre les attaques réitérées de Mr. le Chanoine Blanc (*Tech. Rep.*): Canton du Valais, A. Advocat imprimeur du Canton. https://doi.org/10.3931/e-rara-53036

Vincent, C., Auclair, S., & Le Meur, E. (2010). Outburst flood hazard for glacier-dammed Lac de Rochemelon, France. *Journal of Glaciology*, *56*, 91–100.

Vreugdenhil, C. B. (1994). *Numerical methods for shallow water flows*. Dordrecht: Kluwer Academic Publishers.

Walder, J. S., & Costa, J. E. (1996). Outburst floods from glacier-dammed lakes: The effect of mode of lake drainage on flood magnitude. *Earth Surface Processes and Landforms*, *21*, 701–723.

Walder, J. S., & O'Connor, J. (1997). Methods for predicting peak discharge of floods caused by failure of natural and constructed earthen dams. *Water Resources Research*, *33*, 2337–2348. https://doi.org/10.1029/97wr01616

Walter, F. (2008). *Catastrophes: Une histoire culturelle XVIe–XXIe siècle*. Paris: Seuil.

Werder, M., Bauder, A., Funk, M., & Keusen, H.-R. (2010). Hazard assessment investigations in connection with the formation of a lake on the tongue of Unterer Grindelwaldgletscher, Bernese Alps, Switzerland. *Natural Hazards and Earth System Sciences*, *10*, 227–237.

Westoby, M. J., Glasser, N. F., Brasington, J., Hambrey, M. J., Quincey, D. J., & Reynolds, J. M. (2014). Modelling outburst floods from moraine-dammed glacial lakes. *Earth-Science Reviews*, *134*, 137–159.

Worni, R., Huggel, C., Clague, J. J., Schaub, Y., & Stoffel, M. (2014). Coupling glacial lake impact, dam breach, and flood processes: A modeling perspective. *Geomorphology*, *224*, 161–176.

Wu, W. (2007). *Computational river dynamics*. London: Taylor & Francis.

Yen, B. (2002). Open channel flow resistance. *Journal of Hydraulic Engineering*, *128*, 20–39.